



Pázmány Péter Katolikus Egyetem
Információs Technológiai és Bionikai Kar

TDK Project Report

Mathematical Modelling of Autophagy-Apoptosis Crosstalk

Krisztián Szuppinger
Molecular Bionics Engineering BSc

2025

Supervisors: Bence Hajdú, Dr. Orsolya Kapuy
Internal Consultant: Dr. Attila I. Csikász-Nagy

Abstract

Autophagy is a central catabolic process in eukaryotic cells that ensures cellular homeostasis by degrading damaged or obsolete components. Its dynamic relationship with apoptosis plays a critical role in determining cell fate under various stress conditions, including nutrient deprivation. The dysregulation of either process has been implicated in a range of pathological states, from neurodegenerative diseases to cancer. While many components of these signaling pathways are known, the systems-level, dynamical behaviour of their interaction remains to be poorly understood.

In this work, we present a mathematical model that captures how extracellular glucose starvation drives autophagy activation through cellular energy imbalance. The model builds on a previously published biochemical reaction network (BCRN) describing autophagy–apoptosis dynamics at basal state. We introduce a new energy-sensing module that tracks glucose uptake, ATP production, overall AXP (ATP, ADP, AMP) dynamics, and nucleotide-dependent AMPK activation. The model distinguishes between ATP-, ADP-, and AMP-bound forms of AMPK, enabling a more accurate representation of AMPK regulation under both homeostatic and stress conditions.

Simulations reproduce a biologically realistic multi-phase response to glucose starvation. An initial compensatory phase delays ATP depletion, but this is followed by an inevitable drop in energy charge that activates AMPK. This activation leads to inhibition of mTORC1 and activation of ULK1/2, initiating autophagy. The model captures known experimental features of this signaling cascade and illustrates how metabolic stress propagates through distinct regulatory layers.

The integration of our starvation module into the existing BCRN framework not only enhances the mechanistic realism of that model but also enables personalized simulations of cellular behavior. With accurate measurements of initial protein concentrations, the finalized model can be adapted to reflect individual cellular conditions and used to simulate how pathologies involving autophagy–apoptosis crosstalk—and their potential treatments—affect key regulatory molecules over time. This framework holds strong potential for advancing personalized medicine by allowing medical professionals to create digital twins of patient-specific cellular states to guide personalized treatments.

Acknowledgements



SUPPORTED BY THE EKÖP-25-1 UNIVERSITY RESEARCH SCHOLARSHIP PROGRAM OF THE MINISTRY FOR CULTURE AND INNOVATION FROM THE SOURCE OF THE NATIONAL RESEARCH, DEVELOPMENT AND INNOVATION FUND.

Contents

Abstract	ii
Acknowledgements	ii
1 Introduction	3
1.1 Cell Death Mechanisms	4
1.2 Autophagy	4
1.2.1 Types of Autophagy	5
1.2.2 Stages of Autophagy	6
1.2.3 Regulation of Autophagy	6
1.2.4 Autophagy Induction - Different Stress Inputs	7
1.2.5 Experimental Glucose Starvation and AMPK	8
1.3 Apoptosis	10
1.3.1 Types of Apoptosis	10
1.3.2 Biochemical Connections of Intrinsic Apoptosis and Autophagy	11
1.4 Interplay Between Cell Death Pathways	11
1.4.1 Cross-talk Between Autophagy and Apoptosis	12
1.5 The Systems Biology Approach	14
1.5.1 Chemical Reaction Networks in Biology	14
1.5.2 Relevant Computational Models	15
2 Objectives	18
3 Materials and Methods	20
3.1 Theoretical Methods	20
3.1.1 Model Construction	20
3.1.2 Obtaining Equations from Regulatory Connections	20
3.1.3 Deriving Rate Constants	21
3.1.4 Setting Initial Conditions	22

3.2	Computational Methods	22
3.2.1	Simulation Environment	23
3.2.2	Initial Condition Sampling	23
3.2.3	Statistical Analysis of Basal State Behaviour	23
3.2.3.1	Basal State Simulations and Their Evaluation	24
3.2.3.2	Basal State Correlation and Covariance	24
3.2.3.3	Analysis of Convergence	24
3.2.3.4	Covariance Convergence	24
3.2.3.5	Correlation Convergence	25
3.2.4	Starvation Modeling	26
3.2.4.1	Simulation	26
3.2.5	Evaluation and Optimization of the Simulations	26
4	Results	28
4.1	Mass Action Model of Glucose Starvation	28
4.2	Statistical Analysis of Basal State Model Behaviour	30
4.2.1	Effectiveness of the Initial Condition Sampling Strategy	30
4.2.2	Analysis of Covariance Convergence	30
4.2.3	Analysis of Correlation Convergence	31
4.3	Simulation of Glucose Consumption	32
4.4	Simulation of ATP Production and Consumption	32
4.5	Autophagy Regulation During Starvation	34
4.5.1	AMPK-AXP Dynamics	34
4.5.2	Dynamics of the mTORC1-ULK1/2-AMPK Regulatory Triangle	35
5	Discussion	37
5.1	Representing Accurate AMPK-AXP Dynamics in Glucose Starvation	37
5.2	Consequences of Effective IC Sampling and Convergence	37
5.3	Information Flow in Our Minimal Model and in More Inclusive Ones	38
5.3.1	Propagation of Starvation Signal Throughout Distinct Submodules	38
5.4	Current Limitations and Future Directions	40
5.4.1	Limitations	40
5.4.2	Future Directions and Applications	41
6	Summary	43

References	44
Supplementary	59
6.1 Defined Reactions and Corresponding Rate Constants	60
6.2 Initial Conditions	65

List of Abbreviations

Abbreviations of the model's species.

Short Notation	Full Name
GLUCIN	Intracellular glucose
GLUCOUT	Extracellular glucose - representative of the whole well
GLUT1	Glucose transporter~1
GLUT1,GLUCIN	GLUT1–GLUCIN complex
GLUT1,GLUCOUT	GLUT1–GLUCOUT complex
ATP	Adenosine triphosphate
ADP	Adenosine diphosphate
AMP	Adenosine monophosphate
AMPK	AMP-activated protein kinase
AMPKA	Active (phosphorylated) AMPK
AMPK_ATP	AMPK bound to ATP
AMPK_ADP	AMPK bound to ADP
AMPK_AMP	AMPK bound to AMP
AMPKA_ATP	Active AMPK bound to ATP
AMPKA_ADP	Active AMPK bound to ADP
AMPKA_AMP	Active AMPK bound to AMP
AMPK_t	Sum of inactive AMPK complexes
AMPKA_t	Sum of active AMPKA complexes
LKB1	Liver kinase~B1
PP2A	Protein phosphatase~2A
AMPK_LKB1	AMPK bound to LKB1
AMPK_ATP_LKB1	AMPK–ATP complex bound to LKB1
AMPK_ADP_LKB1	AMPK–ADP complex bound to LKB1
AMPK_AMP_LKB1	AMPK–AMP complex bound to LKB1
AMPKA_PP2A	Active AMPK bound to PP2A
AMPKA_ATP_PP2A	Active AMPK–ATP complex bound to PP2A
AMPKA_ADP_PP2A	Active AMPK–ADP complex bound to PP2A
AMPKA_AMP_PP2A	Active AMPK–AMP complex bound to PP2A
MTOR	Inactive mTORC1
MTORA	Active mTORC1
RHEB	Ras homolog enriched in brain
RHEBA	Active RHEB
TSC	Tuberous sclerosis complex
TSCA	Active TSC (GAP-active form)
ULK	Inactive ULK1/2
ULKA	Active ULK1/2
Q	Proton motive force

General Abbreviations of the Thesis.

Abbreviation	Full expression
AA	Amino acids
ACD	Accidental cell death
ATG	Autophagy-related gene/protein
AXP	Adenine nucleotide pool (ATP, ADP, AMP)
Bcl-2	B-cell lymphoma~2
Bcl-xL	B-cell lymphoma-extra large
BCRN	Biochemical reaction network
CMD	Correlation matrix distance
CRN	Chemical reaction network
cpc	Copies per cell
DMEM	Dulbecco's modified Eagle medium
EBSS	Earle's balanced salt solution
E	Enzyme (Michaelis–Menten)
S	Substrate (Michaelis–Menten)
ES	Enzyme–substrate complex (Michaelis–Menten)
P	Product (Michaelis–Menten)
GH	Growth hormone
IQR	Interquartile range
IP ₃ R	Inositol 1,4,5-trisphosphate receptor
KL	Kullback–Leibler divergence
K _M	Michaelis constant
LC3-I	Cytosolic form of LC3
LC3-II	Phosphatidylethanolamine-conjugated LC3
MIMO	Multiple-input multiple-output
MM	Michaelis–Menten
MOMP	Mitochondrial outer membrane permeabilization
NCI-60	National Cancer Institute 60 cell line panel
ODE	Ordinary differential equation
PCD	Programmed cell death
PE	Phosphatidylethanolamine
PI3K	Phosphoinositide 3-kinase
RV	Escoufier Rho-vector similarity
SSM	State-space model
UVRAG	UV radiation resistance-associated gene
V _{max}	Michaelis-Menten maximum enzymatic rate

Chapter 1

Introduction

Biological cells are sophisticated survival machines, finely tuned by evolution to adapt to and proliferate in an ever-changing environment [1]. This task requires the cell to adequately sense external conditions, integrate them with its internal state, and produce a response that maximizes its survival and/or proliferation rate [2]. From this perspective, biological cells can be viewed as multiple-input multiple-output (MIMO) systems that receive input signals in the form of environmental cues, integrate these with their internal state (which could be, for example, the phase of the cell cycle), and compute an output (i.e., a cellular action). Using this abstract framework, a cell (just like any other MIMO model) can be described by a dynamical systems framework [3]. Consequently, the behaviour of a cell in response to specific input signal(s) is determined by the equations and, more precisely, by the parameters of the dynamical system describing it.

Among the various environmental input signals affecting cellular behaviour, nutrient availability is one of the most fundamental. Biologically, the input of low nutrient levels – or more specifically, starvation – evokes two principal outputs: activation of autophagy as a survival strategy, or initiation of cell death via apoptosis when the stress persists or exceeds the cell’s adaptive capacity [4], [5].

This decision between life and death is one of the most fundamental choices that cells of multicellular organisms must make. Consequently, incorrect decisions e.g., due to dysfunctions in autophagy or apoptosis are associated with various pathologies such as cardiovascular diseases, neurodegeneration, inflammatory disorders, and cancer [6], [7], [8], [9]. For this reason, it is of utmost importance to disentangle these mechanisms, elucidate their regulation, and understand their interconnections. This will not only facilitate the development of effective therapeutic strategies but also deepen our understanding of the aforementioned devastating diseases.

Therefore, the present work aims to establish a quantitative in silico model of autophagy–apoptosis

crosstalk that can guide mechanistic insight and support more precise experimental designs addressing the etiology and progression of these pathologies.

1.1. Cell Death Mechanisms

The death of a cell could either be a tightly regulated response to given stimuli, or the consequence of an accidental event. In the literature, therefore, two categories are distinguished: regulated cell death (RCD) and accidental cell death (ACD) [5], [10].

The archetypal example of ACD is necrosis. This is a rapid and often chaotic form of cell disintegration that occurs when the stress is too severe or too sudden for regulatory processes to engage [11]. Necrosis generally leads to inflammation of the surrounding area, and thus it is a fundamentally disadvantageous process for multicellular organisms [12]. In contrast, RCD represents a controlled, often genetically encoded, sequence of events with the overall goal to prevent inflammation after cellular disintegration [5]. We will discuss two RCD processes: autophagy and apoptosis.

Apoptosis, or programmed cell death (PCD), represents a deliberate cellular self-destruction process orchestrated by caspases, ensuring that the cell is eliminated without triggering inflammation [12]. During apoptosis, the cell fragments into membrane-bound vesicles that are rapidly engulfed by phagocytes, leaving no trace of inflammation [13]. On the other hand, autophagy is a cellular self-degradation mechanism through which cytoplasmic components are transported to lysosomes and degraded following the formation of autolysosomes [14]. This process does not necessarily result in cell death, in fact, its primary role is cytoprotective [4], [5].

Figure 1.1 provides a schematic overview of the aforementioned cell death processes and also indicates some of the key regulator molecules that mediate crosstalk between these processes [15].

1.2. Autophagy

Autophagy is a catabolic stress response that enables cells to adapt to unfavorable conditions. It is typically triggered by nutrient deprivation or other stressors such as hypoxia, oxidative damage, or metabolic imbalance [16], [17]. The term “autophagy” encompasses multiple mechanisms divided into three main categories: macroautophagy, microautophagy and chaperone-mediated autophagy. In this work, we focus specifically on macroautophagy, which we refer to simply as autophagy throughout.

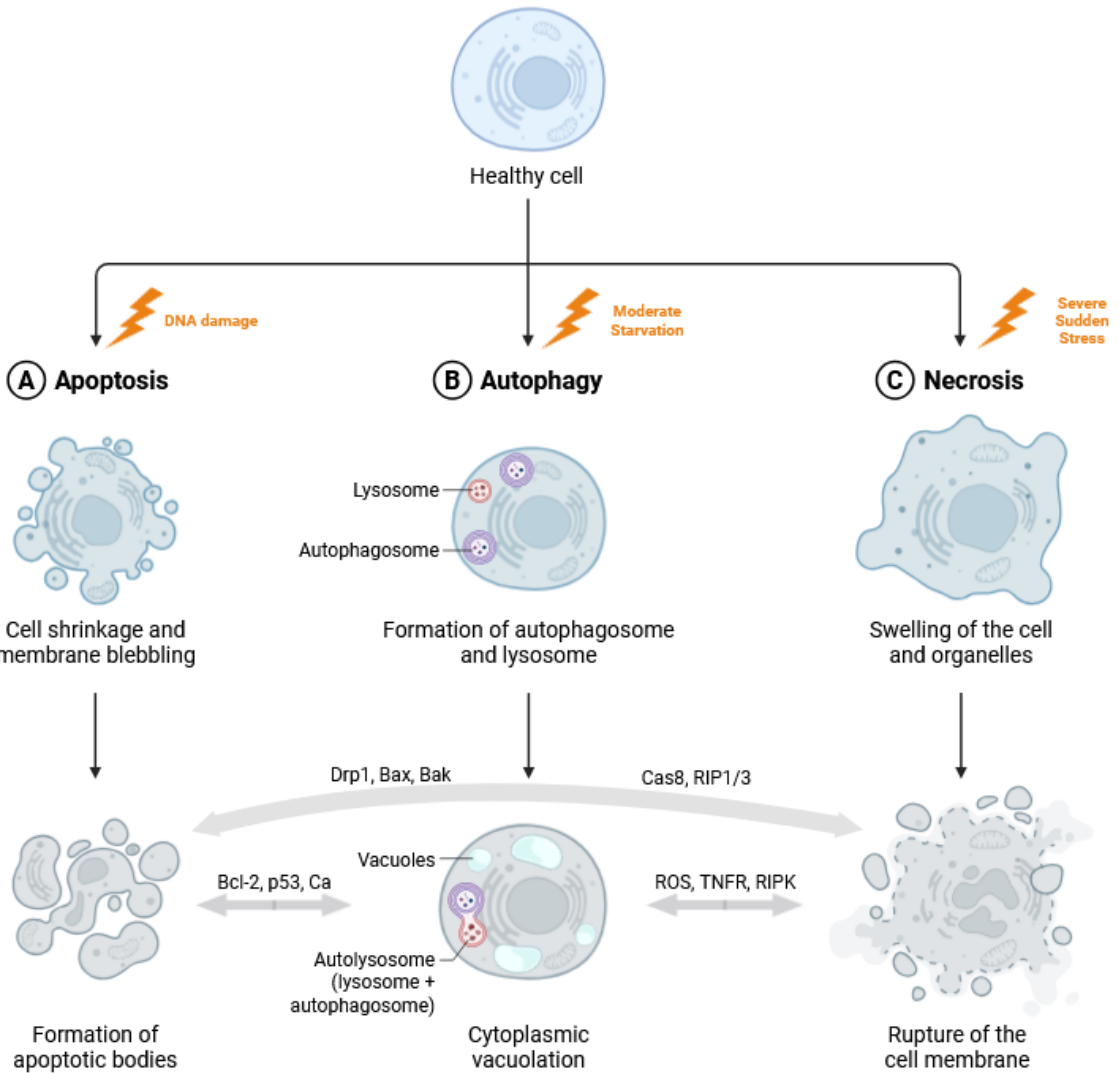


Figure 1.1: Schematic representation of three major cellular responses to different types and levels of stress: apoptosis, autophagy, and necrosis (shown from left to right). Crucially, these pathways are not distinct, but influence each other via an intricate network of common proteins. These connections, along with examples of shared regulator proteins are also provided. The figure was created based on the review of Eskander et al. [15], using this BioRender template

1.2.1 Types of Autophagy

The best-characterized subtype is macroautophagy. This involves the encapsulation of cytoplasmic cargo, such as proteins or organelles, by a double-membrane vesicle originating from the endoplasmic reticulum. This vesicle, known as the autophagosome, subsequently fuses with a lysosome, forming an autolysosome in which the enclosed material is degraded and recycled to sustain essential biosynthetic pathways [16], [18]. Basal autophagy is therefore cytoprotective, maintaining cellular homeostasis by removing misfolded or damaged proteins and organelles, and redistributing their building blocks [19].

Other specialized forms of (macro)autophagy target and recycle specific substrate constituents:

glycophagy mobilizes carbohydrates, lipophagy releases lipids, and ferritinophagy regulates intracellular iron levels [20].

1.2.2 Stages of Autophagy

The autophagic process can be divided into five stages: (i) initiation, (ii) elongation, (iii) completion, (iv) docking and fusion with the lysosome, and (v) degradation [21]. During initiation, portions of the cytoplasm or organelles are sequestered into an isolation membrane that elongates and closes to form an autophagosome (completion). The autophagosome then fuses with a lysosome to create an autolysosome, where hydrolytic enzymes degrade the cargo into fundamental biomolecules. These breakdown products are subsequently released into the cytosol by permeases and reused for anabolic processes [22].

1.2.3 Regulation of Autophagy

Beyond its role as a stress adaptation mechanism, autophagy also regulates physiological processes such as metabolism, cell growth, and survival [23]. This versatility arises from its extensive molecular machinery, coordinated by numerous kinases, phosphatases, and GTPases encoded by autophagy-related genes (ATG) [24].

The central regulators of autophagy include the 5' AMP-activated protein kinase (AMPK), the mammalian target of rapamycin complex 1 (mTORC1), and the Unc-51-like autophagy-activating kinases 1 and 2 (ULK1/2) [25]. Under nutrient-rich conditions, mTORC1 phosphorylates and inactivates the ULK1/2 complex, thereby promoting anabolic processes and cell growth. In contrast, during stress, AMPK activation shifts the cellular balance from biosynthesis toward catabolic degradation. This is because AMPK both directly activates the ULK1/2 complex and disinhibits it by inhibiting mTORC1 [25], [26]. Activating the ULK1/2 complex, as well as releasing it from suppression ultimately leads to the initiation of autophagy [26]. A summary of these interactions is provided in Fig. 1.2.

Following initiation, membrane elongation is mediated by several ATG proteins, while completion of the autophagosome requires the involvement of LC3-II, and fusion is mediated by proteins such as Beclin-1 and UVRAg [27]. Importantly, LC3-II is the phosphatidylethanolamine (PE)-conjugated form of the microtubule-associated protein LC3-I. Once conjugated, LC3-II integrates into the growing isolation membrane, facilitating its elongation and eventual closure to form the autophagosome [28], [29]. Notably, LC3-II itself is degraded within the autolysosome; therefore, monitoring its lysosomal turnover provides a reliable indicator of autophagic activity. Figure 1.3 presents a schematic overview of the autophagy pathway highlighting not only the

stages of autophagy, but also the molecular signaling pathways that might activate the process.

In the next section, we will elucidate how these signaling pathways are abused in experiments to induce autophagy. Three distinct, but connected mechanisms are introduced, with focus placed on the starvation pathway utilizing AMPK as the intracellular nutrient sensor.

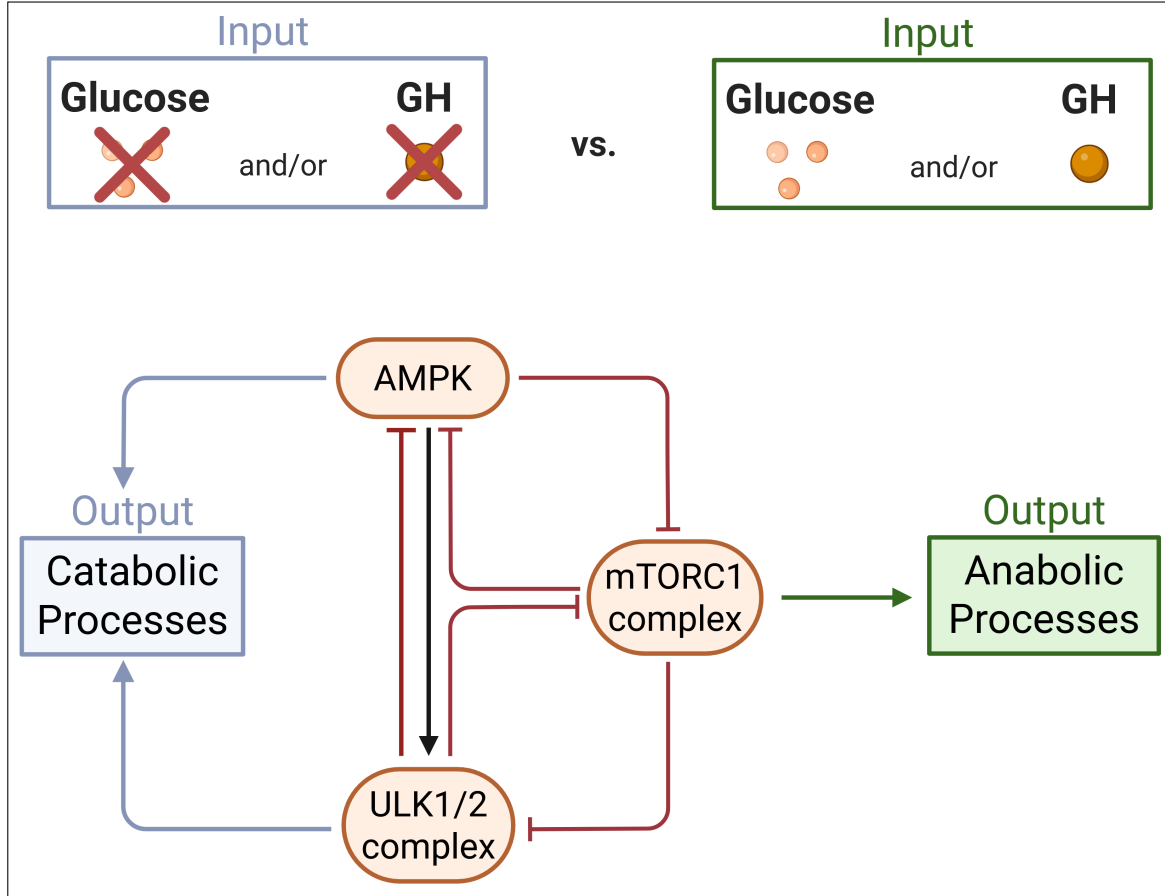


Figure 1.2: Schematic representation of nutrient-dependent regulation of autophagy and anabolic signaling through AMPK, mTORC1, and the ULK1/2 complex. Two distinct input conditions are shown: green panels depict physiological states in which nutrients (e.g., glucose, amino acids, and/or growth hormones, GH) are sufficient, whereas the blue-toned panels illustrate stressed conditions such as nutrient deprivation (e.g., glucose starvation). The core regulatory proteins - AMPK, mTORC1, and ULK1/2 - are shown in red, highlighting their central role in integrating metabolic cues [26], [30], [31]. Red blunt-ended lines indicate inhibitory interactions, while black arrows denote activation. Depending on the input, the system drives either anabolic (green) outputs mediated by AMPK and ULK1/2 activation or catabolic (blue) outputs, induced by mTORC1-mediated suppression of the ULK1/2 and AMPK. The figure was created using BioRender

1.2.4 Autophagy Induction - Different Stress Inputs

As previously discussed, autophagy is a stress response. Consequently, experimental induction of autophagy typically involves exposing cells to specific stress stimuli. These are most often metabolic stresses such as nutrient deprivation or pharmacological treatments that mimic starva-

tion. Famous examples of the latter include the mTORC1 inhibitor rapamycin and the AMPK activator metformin [32], [33]. Additionally, non-metabolic stressors such as DNA damage or hypoxia can also trigger autophagy [34], [35].

The two most frequent autophagy inducers are rapamycin treatment and nutrient starvation. Both are well-established experimental methods to induce autophagy [33], but they differ in how they initiate autophagic signaling. Their basic characteristics are briefly summarized below.

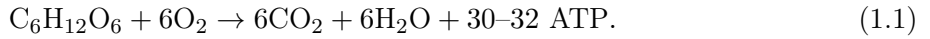
Rapamycin. One of the most extensively studied inducers of autophagy is rapamycin [36], [37]. This compound modulates the kinase-phosphatase balance controlling autophagy by allosterically inhibiting mTORC1. Mechanistically, rapamycin forms a complex with FKBP12 and an mTOR subunit, resulting in mTORC1 inhibition [38]. This inhibition promotes autophagy [39] by facilitating ULK1 dephosphorylation at inhibitory residues such as Ser637 and Ser757 [39], [40].

Starvation. Starvation is a less precisely defined experimental input compared to rapamycin treatment, as its effects depend strongly on the cellular and environmental context [40]. Based on the experimental literature used to generate the time-course data in our work for parameter estimation, three distinct conditions are commonly employed to induce starvation-mediated autophagy: (i) amino acid deprivation, (ii) glucose starvation, and (iii) growth hormone or insulin withdrawal. Figure 1.3 illustrates how these experimental conditions activate autophagy.

In this work, we focus specifically on glucose deprivation, and therefore, in the next section, this starvation pathway is described in more detail.

1.2.5 Experimental Glucose Starvation and AMPK

Extracellular glucose enters the cell via facilitated diffusion mediated by glucose transporters (e.g., Na⁺-glucose cotransporter [44]. Once inside, glucose undergoes glycolysis in the cytoplasm, followed by the Krebs cycle and oxidative phosphorylation in the mitochondria. These processes ultimately produce the primary cellular energy currency, adenosine triphosphate (ATP), according to the reaction:



Based on eq. (1.1), ATP levels are fundamentally controlled by intracellular glucose levels, which - in experimental settings - are influenced by the concentration of glucose in the cell culture media. In physiological circumstances, this concentration amounts to 5.5–7.8 mM [45], [46]. At significantly lower concentrations ($\leq \approx 1.4\text{mM}$), cells begin to show signs of starvation (e.g., active autophagy). If sufficient amounts of glucose are present, ATP is created by phosphoryla-

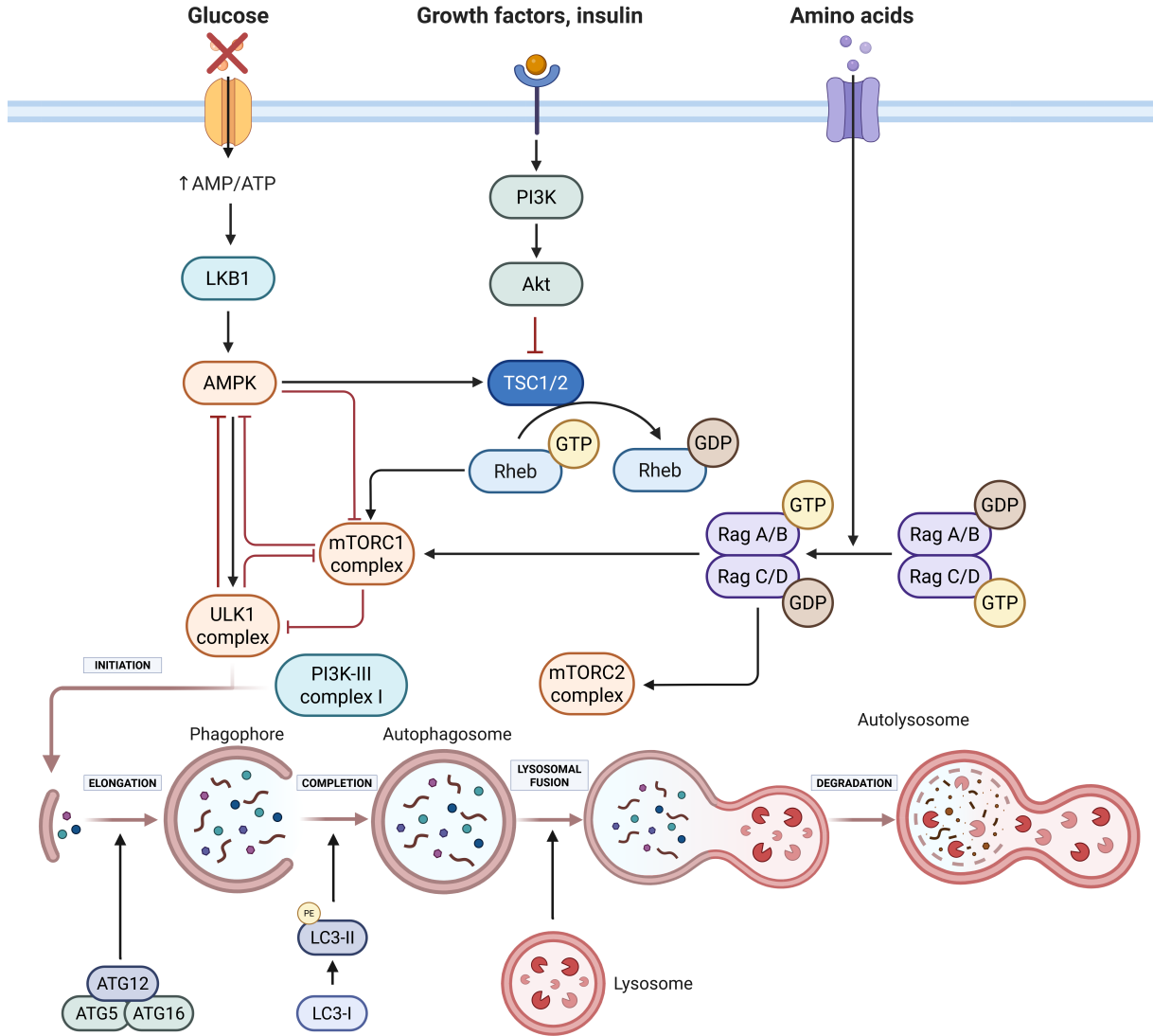


Figure 1.3: Three primary starvation-sensing pathways are depicted. Glucose deprivation decreases ATP production, activating AMPK, which in turn stimulates ULK1 and inhibits mTORC1. Growth factor or hormone withdrawal suppresses PI3K-Akt signaling, leading to mTORC1 inactivation and subsequent AMPK and ULK1 activation. Amino acid (AA) deprivation is commonly modeled using minimal media such as EBSS, DMEM, or DBSS, which contain salts and glucose but lack serum, which is the principal source of amino acids in culture [26], [41], [42], [43]. All three pathways converge on the AMPK-mTORC1-ULK1 regulatory axis, which coordinates phagophore formation, autophagosome maturation, and lysosomal degradation during autophagy. The figure was created based on this BioRender template

tion of adenosine diphosphate (ADP), which itself is generated by phosphorylation of adenosine monophosphate (AMP). These adenosine nucleotides (collectively referred to as AXPs in this work) are then continuously interconverted between each other to maintain sufficient ATP levels [47].

In physiological settings, intracellular ATP concentrations vary rather significantly among different cell types, however, a reasonable range is 2–8 [mM] [48], [49], [50]. ADP and AMP concentrations are significantly lower, approximately 50–200 [μ M] and 0.5–5 [μ M], respectively

[51], [52], [53]. During glucose starvation, however, ATP production decreases, while ADP and AMP levels rise [54]. These altered $[ADP] : [ATP]$ and $[AMP] : [ATP]$ ratios activate AMPK, which phosphorylates downstream targets to promote energy-producing pathways and inhibit energy-consuming ones. Specifically, AMPK facilitates autophagy initiation through ULK1/2 phosphorylation and suppresses proliferation by inactivating mTOR.

AMPK is a heterotrimeric protein complex composed of one catalytic (α) and two regulatory (β and γ) subunits. It becomes several hundred-fold more active upon phosphorylation at Thr172 (or Thr183 in humans) on the α -subunit, mediated by kinases such as CaMKK β or LKB1 [55]. AMPK contains four nucleotide-binding sites, three of which are typically occupied [51]. These sites bind AXPs non-selectively: AMP, ADP, and ATP can all occupy them, although site 4 is preferentially bound by AMP, while the other two are occupied competitively [56].

The binding of ADP or AMP stabilizes the phosphorylated Thr172 state, preventing dephosphorylation and promoting further activation of AMPK. Additionally, AMP binding induces allosteric activation, increasing kinase activity two- to five-fold [51]. In contrast, ATP binding stabilizes the inactive state of AMPK thus it facilitates the dephosphorylation of AMPK by phosphatases such as PP2A. This generally leads to cell growth through mTORC1 disinhibition when energy is abundant [51], [56].

Importantly, AMPK is regulated not only by AXPs, but also by numerous other proteins, such as mTORC1 and ULK1/2. Notably, a Ca^{2+} signaling network protein, CaMKK β also activates AMPK via phosphorylation at Thr¹⁷² [4]. This provides another link between autophagy and apoptosis, as Ca^{2+} signaling via calpain influences apoptotic pathways as well.

1.3. Apoptosis

Apoptosis, or programmed cell death (PCD) is a tightly controlled form of RCD mediated by an intracellular proteolytic cascade primarily driven by caspases [12]. The main goal of PCD is to counterbalance mitosis and to help maintain homeostatic cell numbers in multicellular organisms [10], [13]. To efficiently achieve this, apoptosis can be triggered either by the cell itself, or by external factors.

1.3.1 Types of Apoptosis

Based on where the apoptotic signal originates from, two principal apoptotic pathways are recognized. In the *extrinsic pathway*, extracellular death ligands (e.g., FAS ligand) bind to death receptors, triggering the recruitment of adaptor proteins and activation of caspase-8, which subsequently activates downstream effector caspases. The *intrinsic* or mitochondrial pathway, in

contrast, is initiated by internal stress signals such as DNA damage or metabolic stress. These signals cause mitochondrial outer membrane permeabilization (MOMP), followed by the consequent release of cytochrome c, then apoptosome assembly via Apaf-1, and finally, activation of caspase-9, leading to cell dismantling through executioner caspases [57]. This internally initiated apoptotic pathway is closely linked to autophagy [58].

1.3.2 Biochemical Connections of Intrinsic Apoptosis and Autophagy

The mitochondrial pathway is governed by a delicate balance between pro- and anti-apoptotic members of the Bcl-2 family. Pro-apoptotic proteins such as Bax and Bak promote MOMP and cytochrome c release, while anti-apoptotic members such as Bcl-2 and Bcl-xL prevent it [58]. The autophagy-related protein Beclin 1 interacts with Bcl-2, thereby establishing a direct molecular link between the regulation of autophagy and apoptosis. Bcl-2 can suppress both processes depending on its binding partners: when it sequesters Beclin 1, autophagy is inhibited, and when it associates with the mitochondrial membrane, it prevents cytochrome c release, thereby blocking apoptotic signaling [59], [60], [61].

Figure 1.4 illustrates the interactions among the regulatory proteins of autophagy and apoptosis in more detail, in a network-level representation. Moreover, the figure also highlights that apoptosis integrates additional signaling cascades, such as the calcium and inositol pathways, and interacts extensively with other cellular programs, most notably autophagy [62]. In the next section, therefore, we will further explore the regulatory connections between autophagy and apoptosis.

The balance between the different cell death mechanisms ensures homeostatic cell numbers in multicellular organisms [10] under physiological conditions. To ensure this balance, several links exist between these processes. In the next section, we will briefly explore these connections and their significance.

1.4. Interplay Between Cell Death Pathways

Reinforcing the intuition that in order to maintain homeostatic cell numbers in multicellular organisms, close cooperation between RCD pathways is required, recent studies have revealed extensive signaling interconnections among them [5], [12], [63].

The interplay between autophagy and apoptosis is particularly intriguing. Autophagy is generally cytoprotective, but excessive or dysregulated autophagic flux can drive cell death, either autonomously or by activating apoptotic pathways [64], [65]. This duality underlies its complex roles in disease.

For example, in cancer, autophagy can promote apoptosis and tumor suppression in early stages but may later support tumor cell survival under metabolic stress [66]. Conversely, in neurodegenerative diseases, active autophagy is neuroprotective, preventing the accumulation of toxic aggregates and mitigating apoptotic cell loss [8].

Figure 1.1 provides a schematic illustration of three distinct cellular responses to different physiological conditions. Apoptosis occurs primarily in response to DNA damage, autophagy is activated under moderate nutrient starvation, and necrosis arises from sudden and severe external stress [5], [10], [13]. Crucially, apoptosis and necrosis both result in cellular disintegration, whereas autophagy, aids survival in harsh conditions (such as nutrient-deprived environments).

These contrasting effects illustrate that autophagy and apoptosis are not mutually exclusive but dynamically coupled processes whose relative balance determines cell fate. Understanding the cross-talk among the different pathways, therefore, is of vital importance for the effective treatment of the various diseases that are influenced by autophagy or apoptosis [67], [68], [69].

In the next section, the intricate, interconnected biochemical regulation of autophagy and apoptosis is explored, detailing the communication between the two processes.

1.4.1 Cross-talk Between Autophagy and Apoptosis

Under nutrient limitation or other extracellular stresses, cells of multicellular organisms have a choice to make: they can either attempt to survive in the harsh conditions by recycling their own constituents via autophagy, or commit suicide in a controlled manner via apoptosis [4]. Importantly, however, it has recently been recognized that the cross-talk between autophagy and apoptosis allows for a more dynamic control, where cells usually first attempt to rescue themselves via autophagy and transition into apoptosis only if the harsh conditions persist [64], [70]. This section describes the cross-talk between autophagy and apoptosis that governs this cell fate decision.

In multicellular organisms, the regulatory links between autophagy and apoptosis are evolutionarily advantageous, since they allow for the fine-tuning of life or death decisions in a dynamically changing environment, which clearly provides a selective benefit [57]. It is not surprising, therefore, that although autophagy and apoptosis are mechanistically distinct, their regulatory networks are highly interconnected [71], [72].

This interdependence complicates the understanding of how cells evaluate stress and decide between survival and death [4]. Stressors such as nutrient deprivation, hypoxia, or growth factor withdrawal can trigger either pathway[5], [63]. Evidence suggests that autophagy is predominantly cytoprotective under mild stress [73], but prolonged or severe conditions shift the balance

toward programmed cell death to prevent necrosis and inflammation [74]. Understanding this balance is crucial, as both autophagy and apoptosis are frequently dysregulated in cancer and contribute to tumor progression and therapeutic resistance [75].

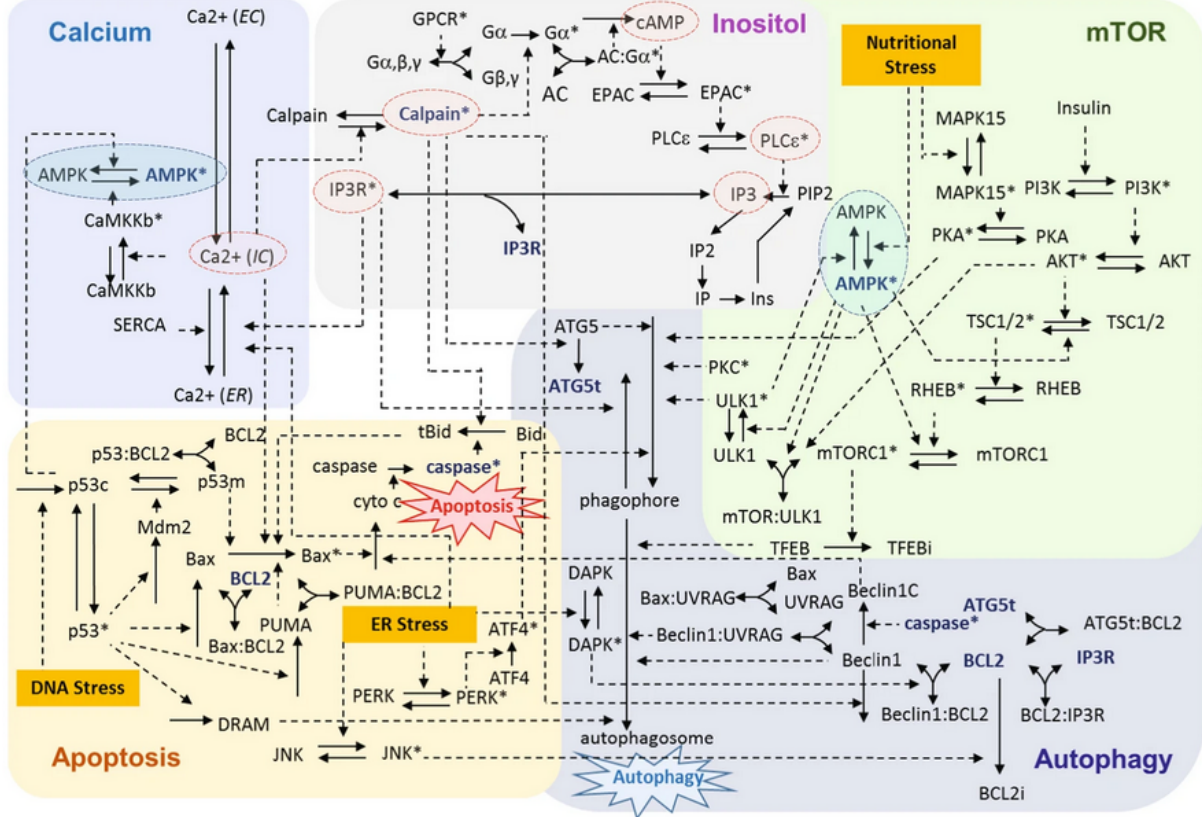


Figure 1.4: Network diagram illustrating interactions among proteins, ions, and metabolites, organized into five interconnected modules: calcium, inositol, mTOR, apoptosis, and autophagy [4]. Solid arrows denote physical interactions (e.g., binding, dissociation, translocation), while dashed arrows represent chemical reactions. Central mediators such as AMPK, IP₃R, Bcl-2, Bax, and Atg5 are displayed in multiple modules to emphasize their multifunctional roles. Key nodes and interactions critical for cell fate decisions are highlighted in red or blue. The three yellow boxes indicate cellular stress inputs, while the starburst shapes denote system outputs corresponding to either autophagy or apoptosis decisions.

As shown in Fig. 1.4, numerous molecular links connect the autophagic and apoptotic machinery. For instance, autophagosome formation is regulated not only by AMPK, mTORC1, and ULK1/2, but also by apoptosis-related proteins such as Beclin1 and Bcl-2. Cross-regulatory interactions include UVrag, which inhibits Bax while promoting autophagy; Bcl-2, which suppresses autophagy by sequestering Beclin1; and caspases, which cleave Beclin1 to shift signaling toward apoptosis. Calcium signaling also bridges the two processes: cytosolic Ca²⁺ levels influence AMPK via CaMKKβ, while simultaneously modulating Bax activity and cytochrome c release. Likewise, the inositol signaling pathway provides an additional link, as calpain affects both phagophore formation and Bax activation through tBid-mediated mechanisms.

Overall, the extensive molecular cross-talk between autophagy and apoptosis makes it challenging to delineate clear boundaries between the two pathways. These network-level complexities, however, are precisely the type of phenomena that systems biology approaches can help unravel [76].

In the following section, the systems-level modeling perspective will be introduced as a quantitative framework for understanding how cells integrate diverse signals to make life-death decisions.

1.5. The Systems Biology Approach

Systems biology seeks to understand biological mechanisms and processes on the network level, focusing not only on local interactions (as traditional reductionist approaches would), but also on emergent properties of the whole system [77]. More rigorously, systems biology is a mathematical framework that applies the tools of dynamical systems theory to analyze networks in a biological context [78]. A modeled cellular process or signaling network can be formulated as a *state-space model* (SSM) [79], [80]. A SSM is a general representation of a system that receives an input and produces an output. Within the system, the dynamics are captured by state variables and their associated differential equations, known as the *state equations*. The system output at any given time is then computed as a function of these state variables.

In a biological context, the input may represent the activating factor(s) of a signaling pathway, while the state variables correspond to the concentrations of proteins or other molecules involved in that pathway. The output might be the concentration of an indicator molecule, such as LC3-II in the case of autophagy.

1.5.1 Chemical Reaction Networks in Biology

Biological cells, as well as signaling networks, can be expressed as systems (and thus as SSMs) using, for example, the *chemical reaction network* (CRN) framework [81]. In this framework, the network of proteins is represented as a directed graph, where the nodes correspond to chemical species (e.g., proteins), and the edges correspond to reactions between them. Each edge is assigned a rate constant k defined by the law of mass action. The resulting formulation yields a system of ordinary differential equations (ODEs), each describing the rate of change of a species' concentration as a function of its interactions and corresponding k values [81], [82].

Computational approaches based on CRNs are powerful tools for understanding complex biological signaling networks, especially as computational resources continue to grow [83], [84]. However, biochemical CRN (BCRN) models face a fundamental challenge: the reaction rate con-

stants are often unknown or difficult to measure accurately [85], [86]. Moreover, these parameters are not strictly time-invariant, as they may depend on changing cellular or environmental conditions [87], [88].

To overcome these limitations, data-driven statistical methods are typically employed to fine-tune model parameters and to implement realistic *in silico* BCRN models [89]. This requires experimental data containing time-course measurements of the relevant state variables, which in turn enable parameter estimation and optimization directly from biological observations. Thus, the systems biology workflow integrates both theoretical modeling and experimental validation in a complementary and iterative manner. This general workflow, as devised by Villaverde et al. [90], is summarized in Figure 1.5.

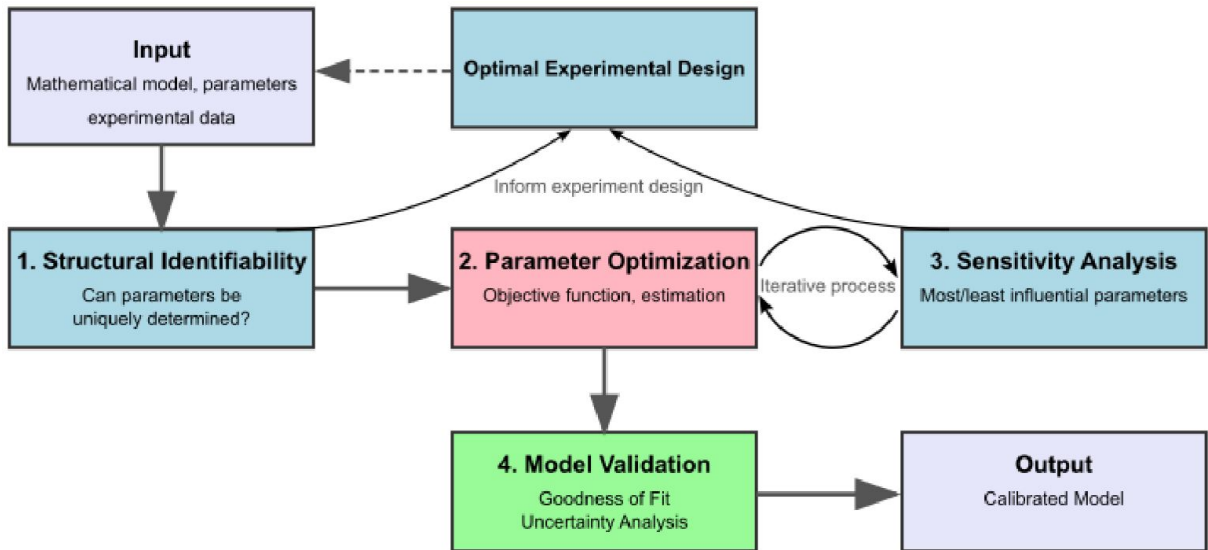


Figure 1.5: First, the model structure is defined, along with the initial parameter estimates, and experimental data. An optimal experimental design ensures the generation informative datasets for parameter estimation. The next steps in calibration are: (i) structural identifiability analysis, (ii) parameter optimization, (iii) sensitivity analysis, and (iv) model validation via goodness-of-fit and uncertainty assessment. Following these steps yields a validated model that is ready for predictive applications [90].

In the following section, general modeling strategies relevant to the systems biology of autophagy are introduced, highlighting their advantages and limitations. This is followed by a description of the *in silico* models that supported the implementation of our model.

1.5.2 Relevant Computational Models

Besides AMPK and mTOR, there is a myriad of other proteins that influence autophagy dynamics. As described previously, complex regulatory networks can be better understood using a computational approach. For this reason, several models of autophagy have previously been implemented, describing the dynamics of a system of proteins.

This section provides a concise overview of the modeling strategies used in autophagy research, followed by a description of the specific models relevant to our starvation-focused simulations.

Common Simplifications Models of autophagy vary in their complexity, the number of proteins, and overall simplification levels. Since the primary aim of most biological models is to capture the dynamic behavior of key species within a molecular network, simplifications are often not a serious problem, as they ideally do not change the dynamics qualitatively. For instance, even a model where the species are represented by artificial units can produce qualitatively meaningful results, and this also simplifies parameter estimation. Tavassoly et al. for example, demonstrated that even without directly measurable concentrations, simplified dynamic models can provide valuable insights into system behavior [76].

On the contrary, BCRN models (i.e., those implemented in this work) provide a quantitative description of the network behavior. Here, the system is represented as a graph where nodes correspond to molecular species, and edges represent reactions weighted by mass-action rate constants. Since these models are generally quantitative, choosing the right initial conditions and parameters is of particular importance and is a task that often requires advanced mathematical approaches [81]. The simplification of BCRN models lies in the assumption that simple mass-action kinetics, even though alternative formulations - such as Michaelis-Menten or Hill kinetics - may capture specific nonlinear behaviors more accurately [81].

While simplified models help identify core principles, more detailed BCRN formulations are necessary to describe the molecular mechanisms underlying autophagy-apoptosis regulation with higher fidelity. This leads to the next extensive model, by Liu et al. which aims to integrate these processes quantitatively.

A Model of Autophagy-Apoptosis Cross-talk. One of the most comprehensive BCRN-based models of autophagy-apoptosis interaction was developed by Liu et al. [4]. However, this model produced unrealistic steady-state behavior, predicting elevated autophagy and apoptosis even under non-stress conditions [81]. To address this limitation, Hajdu et al. restructured the system of equations, refined key kinetic parameters, and reduced the number of molecular species from 94 to 84. Additionally, concentration ranges were derived from the literature for 34 of the 84 species, which were then used as performance indicators for model validation. The wiring diagram of the original Liu et al. model is shown in Figure 1.4.

This restructured, optimized model represented a strong foundation and an accurate description of the basal-state dynamics. However, it lacked clear, stress specific input mechanisms, such as glucose deprivation. Therefore, in order to expand the regulatory scope of our framework, we

sought additional models that contained such input mechanisms.

Models of AMPK Dynamics and Glucose Starvation. For this work, we focused on the dynamic properties of three key processes: (1) glucose transport into the cell, (2) glucose metabolism and ATP production, and (3) AMPK regulation by adenosine nucleotides.

The model by Zhou et al. [91] was employed to describe glucose transport. This framework simulates glucose starvation and its effects on AMPK, mTOR, p53, and Akt signaling. The original model that assumed glucose uptake occurred primarily through GLUT1 transporters. Furthermore, an important simplification of this model is that the simulated concentrations of the species are expressed in arbitrary units.

Coccimiglio et al. [92], devised a model to characterize AMPK activity in human skeletal muscle cells. This model consists of 17 species governed by 17 ODEs derived from 25 reactions, with specific emphasis on ADP/ATP/AMP binding affinities. Although optimized for muscle physiology during exercise rather than starvation, its parameters provided a reasonable foundation for re-optimization in our context of glucose deprivation and thus this model was used as the basis of our AMPK-AXP dynamics.

Collectively, these existing models form the conceptual and quantitative foundation of our extended framework. By combining insights from autophagy-apoptosis regulation with those from glucose- and AMPK-related dynamics, our integrated BCRN model aims to capture cellular decision-making under nutrient stress in a unified and mechanistically consistent manner.

Chapter 2

Objectives

This research aims to elucidate the dynamical mechanisms that induce autophagy under glucose starvation. The work forms an integral part of the broader effort to construct an *in silico* model describing autophagy–apoptosis crosstalk. The potential applications of this work span from foundational systems biology research to personalized medicine and patient-specific drug design. The specific objectives of this work are:

- 1. Construction of a biologically plausible *in silico* BCRN model for glucose starvation**
 - (a) Devise a biologically authentic wiring diagram that implements glucose starvation and integrates into the existing framework of a basal state BCRN model.
 - (b) Review the literature to derive the rate constants that define the ODEs governing the BCRN, as specified by the law of mass action.
 - (c) Identify physiological initial concentration values for the species of the BCRN.
- 2. Conduct a statistical analysis of the network’s basal state behaviour**
 - (a) Assess the effectiveness of the derived initial conditions in producing quasi-stationary outputs that remain within well-defined physiological concentration ranges.
 - (b) Analyze the covariance and correlation of the basal state dynamics and assess convergence of the matrices
- 3. Analyze the behaviour of the implemented, basally stable model during starvation**
 - (a) Fine-tune and evaluate the model’s accuracy in representing the effects of insufficient extracellular glucose concentrations, including validation of glucose and ATP consumption rates for biological plausibility.

- (b) Explore the model dynamics of the autophagy-related proteins AMPK, mTORC1, and ULK1/2 under glucose starvation and cross-reference the results with the literature.
- (c) Confirm that nutrient scarcity inputs are correctly propagated from glucose dynamics through AXP-mediated AMPK activation toward the autophagy regulatory triangle comprising AMPK, mTORC1, and ULK1/2.

Chapter 3

Materials and Methods

3.1. Theoretical Methods

This section details the literature review process that guided the construction of the basic wiring diagram of our BCRN. Furthermore, the procedures used to infer rate constants and initial conditions characterizing the governing ODEs are also elucidated.

3.1.1 Model Construction

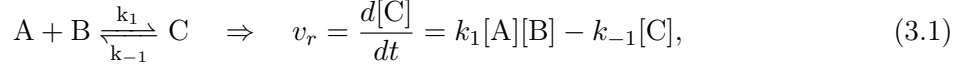
The wiring diagram of the implemented network was defined after a thorough literature review. Key proteins and regulatory molecules involved in starvation-induced autophagy were identified. Three distinct sources were used to implement most of the reactions defined in the model. ODEs describing glucose transport and metabolism were adapted from the in silico starvation model of Zhou et al. [91]. Coccimiglio et al.’s detailed model of AMPK dynamics informed the AXP–AMPK (ATP/ADP/AMP–AMPK) submodule [92]. Finally, Hajdu et al.’s work [81] was used to connect starvation-induced stress to autophagy and apoptosis via mTORC1 and ULK1/2.

Consequently, in the model, inactive AMPK complexes (i.e., AMPK_ATP, AMPK_ADP, AMPK_AMP, and AMPK), active mTORC1 (MTORA), and inactive ULK1/2 (ULK) represent homeostatic conditions. Conversely, activation of AMPK (AMPKA_ATP, AMPKA_ADP, AMPKA_AMP, and AMPKA), inhibition of mTORC1 (MTOR), and activation of ULK1/2 (ULKA) define an autophagic-like state.

3.1.2 Obtaining Equations from Regulatory Connections

The law of mass action was employed to define the governing equations of the BCRN. For a reversible reaction with two reactants A and B forming C, the relationship between concentrations

and the reaction rate v_r is given in the form of eq. (3.1).



where $[A]$, $[B]$, and $[C]$ are species concentrations, while k_1 and k_{-1} are the forward and reverse rate constants, respectively. The reactions (and corresponding ODEs) in our BCRN follow this framework and are provided in the Supplementary Material 6. The contributions drawn from Zhou et al., Coccimiglio et al., and Hajdu et al. are also highlighted there.

3.1.3 Deriving Rate Constants

The k rate coefficients are either taken directly from prior work or inferred from experimental or computational sources. In several cases (notably in Coccimiglio et al. [92] and Zhou et al. [91]), kinetic parameters are given in Michaelis–Menten (MM) form (V_{\max} , K_M) and must be mapped to elementary mass-action rates.

The equations describing an enzymatic reaction with MM kinetics for an enzyme E, substrate S and product P are given in eq. (3.2). The corresponding MM formulation of the initial reaction speed V_0 is also provided.



with ES the transient complex and initial amounts $[E_0]$, $[S_0]$, $[P_0]$. Decomposing (3.2) gives the elementary mass-action ODEs:

$$\left. \begin{array}{l} E + S \xrightarrow{k_1} ES, \\ ES \xrightleftharpoons{k_{-1}} E + S, \\ ES \xrightarrow{k_2} E + P \end{array} \right\} \iff \left\{ \begin{array}{l} \frac{d[S]}{dt} = -k_1[E][S] + k_{-1}[ES], \\ \frac{d[E]}{dt} = -k_1[E][S] + (k_{-1} + k_2)[ES], \\ \frac{d[ES]}{dt} = k_1[E][S] - (k_{-1} + k_2)[ES], \\ \frac{d[P]}{dt} = k_2[ES]. \end{array} \right. \quad (3.3)$$

Given K_M and V_{\max} , we recover a physically meaningful mass-action set by fixing the ratio $\alpha \equiv k_2/k_{-1}$ (relative catalytic efficiency). Then the rate coefficients and $[E_0]$ are:

$$k_1 = \frac{k_{-1}(1 + \alpha)}{K_M}, \quad k_2 = \alpha k_{-1}, \quad [E_0] = \frac{V_{\max}}{k_2}. \quad (3.4)$$

3.1.4 Setting Initial Conditions

A feasible range r of initial concentrations (IC) x , applicable to physiological conditions is defined based on experimental or modeling data. For each species s of the model between a lower bound lb and an upper bound ub : $s_r = [x_{lb}, x_{ub}]$. A mean value \bar{x} is defined for each range as well, representing typical values found in the literature. Initial values for intermediate complexes are set to near 0, in the range of $\approx 10^{-14} \frac{mol}{cm^3}$.

For species, LKB1, PPA2, and GLUT1, ICs are derived from mass-spectrometry (MS) data. Following Wiśniewski et al.'s "proteomic ruler" [93] and related large-scale cell-line proteomes (e.g., NCI-60 SWATH, pan-cancer atlases [94]), per-cell copy numbers can be estimated and converted to molar concentrations.

If cpc denotes copies per cell of protein X, then with Avogadro's number N_A and mean cell volume V_{cell} $[X]$ is given as follows eq. (3.5)

$$M = \frac{n_X}{V_{cell}} \Rightarrow [X] = \frac{cpc}{N_A \times V_{cell}} \quad (3.5)$$

where n_X is the amount of the protein inside the cell in moles.

In online databases such as PaxDB, the available MS data is measured in units of ppm. According to Wisniewsky et al., this can be converted to cpc if the molar mass M_X of the protein X and the total mass of all proteins in the cell m_{prot} are known. If this is the case, then cpc and thus concentrations can be derived from MS ppm data as follows (3.6).

$$cpc = ppm \times m_{prot} \times \frac{N_A}{M_X}, \quad [X] = \frac{ppm \times m_{prot}}{M_X V_{cell}}. \quad (3.6)$$

Based on the available literature, in our calculations, we set $m_{prot} = 464 \pm 35$ [pg], $V_{cell} = 1$ [cm^3] and $ppm = (\text{measured data}) \pm 0.2 \cdot (\text{measured data})$ [93].

3.2. Computational Methods

The section describes the computational and statistical methods employed in this work. The simulation environment used for numerical calculations, data analysis methods, quantification techniques for model convergence, and model evaluation metrics are also detailed. Additionally, a figure, summarizing our workflow and the pipeline of the employed methods is also provided in Fig. 3.1.

3.2.1 Simulation Environment

The system of ODEs defined by mass action (Sec. 3.1) governs the BCRN’s temporal dynamics. Numerical integration uses the CANTERA solver within the Optima++ environment to solve this system of differential equations. Cantera is a popular solver for problems in chemical reaction kinetics [95]. Optima++, on the other hand, is a simulation environment originally developed for describing and optimizing temperature-dependent Arrhenius parameters ($k(T) = AT^n e^{-E/RT}$) of large-scale combustion kinetics networks [96] [97]. However, Optima++ can be employed to model isothermal biological simulations (such as those implemented in this work) by setting the rate coefficients temperature-independent.

3.2.2 Initial Condition Sampling

For the simulation of dynamical systems, the initial conditions (ICs) describing the system at $t = 0$ are crucial. In this model, the concentrations of species at $t = 0$ are sampled from the ranges outlined in 3.1.4.

The sampling strategy employed is informed by and based on our previous work (available at the *Online Supplementary Material* under ‘Prerequisites’). For each variable s , in our model, the corresponding IC is randomly generated from a uniform distribution. The range of values in this distribution is not the same as the concentration ranges s_r mentioned in 3.1.4. Rather, the sampling range for species s is defined as follows: $[0.5 \cdot \bar{x}_s, 1.5 \cdot \bar{x}_s]$. We set the standard deviation (std) to $|\sigma^{(s)}| = 1/8 \cdot ||0.5 \cdot \bar{x}_s, 1.5 \cdot \bar{x}_s||$ and fix the random seed for reproducibility.

Importantly however, the concentrations of extracellular glucose (GLUCOUT) defines the primary stress input of the model and thus it is set deterministically. In our framework, a physiological state uses $\text{GLUCOUT} = 6 \cdot 10^{-6} \frac{\text{mol}}{\text{cm}^3}$, while starvation corresponds to $\text{GLUCOUT} = 1 \cdot 10^{-6} \frac{\text{mol}}{\text{cm}^3}$ [45].

The sampling ranges set according to the available literature for all species of the model are provided in Supplementary Table 6.2. For both basal and starvation conditions, the ICs are sampled according to the same method, meaning that we assume that the cells were kept in physiological conditions before a given starvation experiment starts.

3.2.3 Statistical Analysis of Basal State Behaviour

To investigate the biological reliability and stability of the designed model, we performed a statistical analysis of the basal state behaviour of the simulated system.

3.2.3.1 Basal State Simulations and Their Evaluation

The randomly generated ICs are saved into an xml file, which will serve as the input of the Optima++ environment. 14 species, out of 38 in the model, are defined as the predictors of the biological plausibility of the model output. The concentration ranges of these descriptor variables inform whether the cell is in a homeostatic environment. The predictors are as follows: MTOR, MTORA, AKT, AKTA, RHEB, RHEBA, TSC, TSCA, ULK, ULKA, AMPK, AMPKA, ATP, and GLUCIN. The full names of these molecules can be found in the list of abbreviations in Section . For modeling, we generate a 24-h reference time series of mean values for these 14 species. This serves as the 'measurements' which Optima++ tries to approximate. The result of a simulation is accepted and used for further statistical analysis if all 14 outputs remain within a 4σ radius of their respective means. We report the acceptance rate as the percentage of XMLs satisfying this criterion. This allows for a simple evaluation metric for a given IC sampling strategy that we denote the 'effectiveness percentage': $\text{eff\%} = \frac{\text{number of accepted xmls}}{\text{number of total xmls}} \cdot 100\%$.

3.2.3.2 Basal State Correlation and Covariance

From a total of 20000 different xmls (all with different ICs) approved xmls are used to compute correlation and covariance matrices of the model's basal state output in Python. The matrices are computed for 27 selected predictors that include the chosen descriptors of the homeostatic state: MTORA, ULK, and AMPK. For the names of all of the predictors, please refer to Supplementary Table 6.2.

3.2.3.3 Analysis of Convergence

The convergence of basal state dynamics was assessed based on the correlation and covariance matrices. Convergence is assessed by tracking distances between correlation/covariance matrices estimated from an increasingly large subset of xmls ($= N_{\text{cond}}$). We assume that if the distance between the matrices decreases as N_{cond} increases, then the two matrices approach the same matrix as $N_{\text{cond}} \rightarrow \infty$. For both covariance and correlation, distances were computed for 6 different xml counts: 50, 450, 1000, 3000, 5500, and 9821.

3.2.3.4 Covariance Convergence

Since the distance metrics used for covariance comparison require the matrices to be positive definite, we first ensure this condition by applying the Ledoit–Wolf shrinkage transformation [98], as shown in eq. (3.7).

$$\hat{\Sigma}_n^* = (1 - \gamma_n) \hat{\Sigma}_n + \gamma_n \hat{\mu}_n \mathbf{I}_n, \quad \text{with} \quad \hat{\mu}_n = \langle \hat{\Sigma}_n, \mathbf{I}_n \rangle = \frac{1}{s} \sum_{i=1}^s \sigma_{ii}^{(n)} \quad (3.7)$$

Here, $\hat{\Sigma}_n$ is the sample covariance matrix - estimated from a sample of size n - with dimensions $(s \times s)$. $\hat{\Sigma}_n^*$ then, is the shrunk sample covariance. \mathbf{I}_n is the identity matrix, and s is the number of variables. The critical parameter is the *shrinkage* coefficient γ_n . The choice of γ_n is such that it minimizes the squared Frobenius-norm ($\|\mathbf{D}\|_F = \sqrt{\sum_{i=1}^n \sum_{j=1}^n |d_{ij}|^2}$) of the error between the true covariance Σ_n and the estimated one $\hat{\Sigma}_n$ [99].

Following this, the Affine-Invariant Riemannian Metric (AIRM) (3.8) can be calculated to assess matrix distances [100]. The AIRM metric is defined as follows (3.8):

$$d_{12}^{\text{AIRM}}(\Sigma_1, \Sigma_2) = \left\| \text{Log} \left(\Sigma_1^{-1/2} \Sigma_2 \Sigma_1^{-1/2} \right) \right\|_F = \left(\sum_{c=1}^C \log^2 \lambda_c \right)^{1/2}, \quad (3.8)$$

where, Log is the matrix logarithm, and the λ_c eigenvalues correspond to the argument of $\text{Log}()$. The greater the value of d_{12}^{AIRM} , the more different the two matrices are.

Covariance distances primarily describe distribution distances, and thus, in addition to the AIRM metric, we also calculate the Kullback-Leibler (KL) divergence (3.9), which specifically quantifies differences between probability distributions [101]. The KL metric is derived from the Shannon entropy formula: $f(x) = x \log(x)$, and is thus also known as the relative entropy [100]. The KL formula:

$$d_{12}^{\text{KL}}(\mathcal{N}_1(\mu_1, \Sigma_1) \| \mathcal{N}_2(\mu_2, \Sigma_2)) = \frac{1}{2} \left(\log \frac{|\Sigma_2|}{|\Sigma_1|} + \text{tr}\{\Sigma_2^{-1} \Sigma_1\} + (\mu_2 - \mu_1)^\top \Sigma_2^{-1} (\mu_2 - \mu_1) - n \right) \quad (3.9)$$

Here, $\mathcal{N}_1(\mu_1, \Sigma_1)$ $\mathcal{N}_2(\mu_2, \Sigma_2)$ are both n dimensional normal distributions, with $\mu_i = \vec{\mu}_i$ as the mean vector, and Σ_i as the covariance matrix. This formulation of the metric thus assumes normal distribution, which - according to the central limit theorem - should not be a problem for high N_{cond} values, but could cause instability in matrices computed from smaller xml counts. Importantly, when we calculate KL divergence values, we first scale the matrices from units of $\frac{\text{mol}}{\text{cm}^3}$ to μM in order to avoid numerical instabilities.

3.2.3.5 Correlation Convergence

For correlation matrices R_1 and R_2 , the correlation matrix distance (CMD) metric [102] was the primary tool of quantifying distances. The definition of CMD is provided in eq. (3.10).

$$d_{12}^{\text{CMD}}(\mathbf{R}_1, \mathbf{R}_2) = 1 - \frac{\text{tr}\{\mathbf{R}_1 \mathbf{R}_2\}}{\|\mathbf{R}_1\|_F \|\mathbf{R}_2\|_F} \in [0, 1], \quad \text{where } \mathbf{R}_i \text{ is the correlation matrix.} \quad (3.10)$$

d_{12}^{CMD} is zero if the two correlation matrices are identical (up to scaling), and one if they are completely orthogonal (since the trace - $\text{tr}\{\cdot\}$ - would be 0).

To complement the CMD metric, we also computed the Rho-vector (RV) coefficient, which is a multivariate extension of the squared correlation originally proposed by Escoufier et al. The RV coefficient quantifies the similarity between two correlation matrices by comparing their overall patterns of covariation rather than individual entries [103]. Its definition is given in eq. (3.11):

$$d_{12}^{\text{RV}}(\mathbf{R}_1, \mathbf{R}_2) = \frac{\text{tr } \mathbf{R}_1 \mathbf{R}_2}{\sqrt{\text{tr } \mathbf{R}_1 \mathbf{R}_1; \text{tr } \mathbf{R}_2 \mathbf{R}_2}}. \quad (3.11)$$

The RV coefficient takes values in $[0, 1]$, where 1 indicates that the two matrices share an identical correlation structure (up to scaling), while values approaching 0 imply increasingly divergent correlation patterns. Unlike the CMD metric, this measure reflects the global organisation of correlations rather than the alignment of matrices in Frobenius space alone [103]. Therefore, the RV coefficient serves as a robust complementary measure to CMD.

3.2.4 Starvation Modeling

3.2.4.1 Simulation

Time courses are computed using Optima++ as described in sections 3.2.1 and 3.2.3.1. The simulations run from $t = 0$ to 84 hours with outputs every 0.5 hours. The time profiles for GLUCOUT, GLUCIN, ATP, ADP, AMP, MTOR, MTORA, ULK, ULKA, as well as for AMPK and AMPKA complexes are plotted using Python. The codes used for this and all other data analysis in this project are available at the *Online Supplementary Material*.

3.2.5 Evaluation and Optimization of the Simulations

In the absence of high-resolution quantitative time-course data, we compare general tendency of the dynamics against Western blots and accept simulations whose trajectories remain biologically plausible and qualitatively consistent with experiment. For glucose dynamics, we additionally assess goodness-of-fit visually and via squared error using the data of Shin et al. [45].

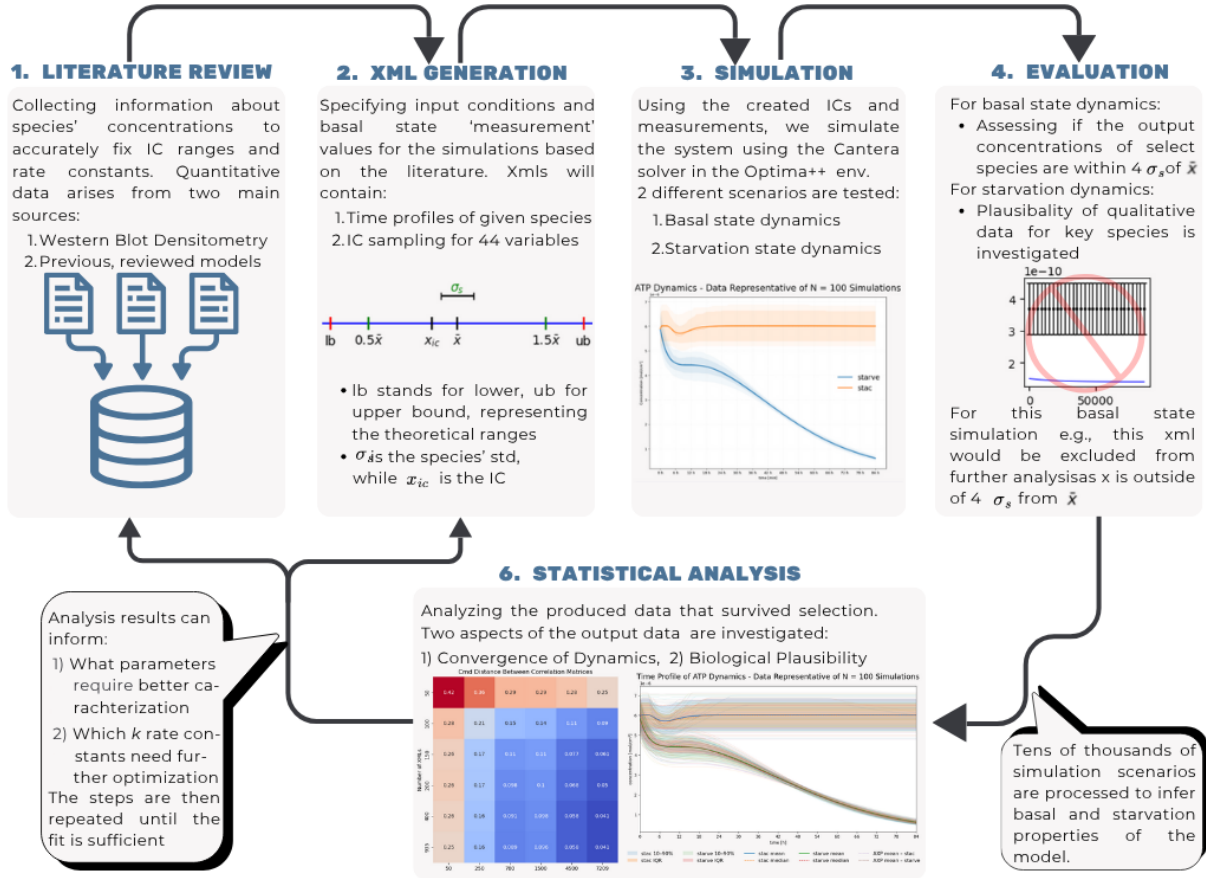


Figure 3.1: The figure provides an overview of the computational workflow used to construct, simulate, and evaluate the biochemical reaction network (BCRN). The process begins with a literature review (Step 1), where concentrations, rate constants, and regulatory interactions are compiled from Western blot experiments and previously published models. These data inform the generation of XML input files (Step 2), in which initial conditions and basal-state "measurement" profiles are specified. Using these XMLs, the system is simulated in Optima++ with the Cantera solver (Step 3) under both basal and starvation conditions. The resulting trajectories are then evaluated (Step 4) to ensure that key species fall within biologically plausible ranges for either a basal or a starvation state. The XMLs that produce qualitatively unreasonable results for starvation conditions or fail the 4σ criterion for basal state simulations are excluded from further analysis. Approved simulations, however, undergo statistical analysis (Step 5–6), including the assessment of dynamical convergence, as well as the investigation of covariance and correlation structure. Insights from this analysis inform subsequent refinement of initial conditions and kinetic parameters, forming an iterative loop (similar to Fig. 1.5 from section 1.5) guiding the optimization of the model.

Chapter 4

Results

4.1. Mass Action Model of Glucose Starvation

To describe glucose-starvation-induced autophagy, firstly, a mass-action biochemical reaction network (BCRN) model was constructed. The model is organized into four submodules that jointly capture glucose uptake and metabolism and propagate the resulting energy-state changes into the autophagy machinery. The model consists of four submodules: 1) glucose metabolism, 2) ATP consumption, 3) AMPK-AXP communication and 4) ULK1-mTOR submodule.

Extracellular glucose (GLUCOUT) enters the cell via facilitated transport mediated by the glucose transporter GLUT1. The imported intracellular glucose pool (GLUCIN) is rapidly consumed through glycolysis, generating ATP via phosphorylation of ADP. The breakdown of intracellular glucose increases the proton motive force (Q), which further enhances ATP production.

ATP is continuously hydrolysed to ADP, which can be further converted to AMP. An AXP cycling reaction is included, in which 2 ADP molecules regenerate 1 ATP and 1 AMP. All three adenine nucleotides can bind to AMPK, forming distinct complexes: AMPK_ATP, AMPK_ADP, AMPK_AMP. The activation state of each complex is determined by phosphorylation and not the bound nucleotide: phosphorylated AMPK species are considered active regardless of which nucleotide is bound, whereas unphosphorylated species remain inactive. Phosphorylation of AMPK is catalysed by LKB1, whereas the phosphatase PP2A mediates its dephosphorylation. For AMPK_ADP and AMPK_AMP, the phosphorylated states are defined to be more stable, whereas for AMPK_ATP, the opposite holds. Conversely, rising values of AMP:ATP or ADP:ATP due to starvation increase overall AMPK activity.

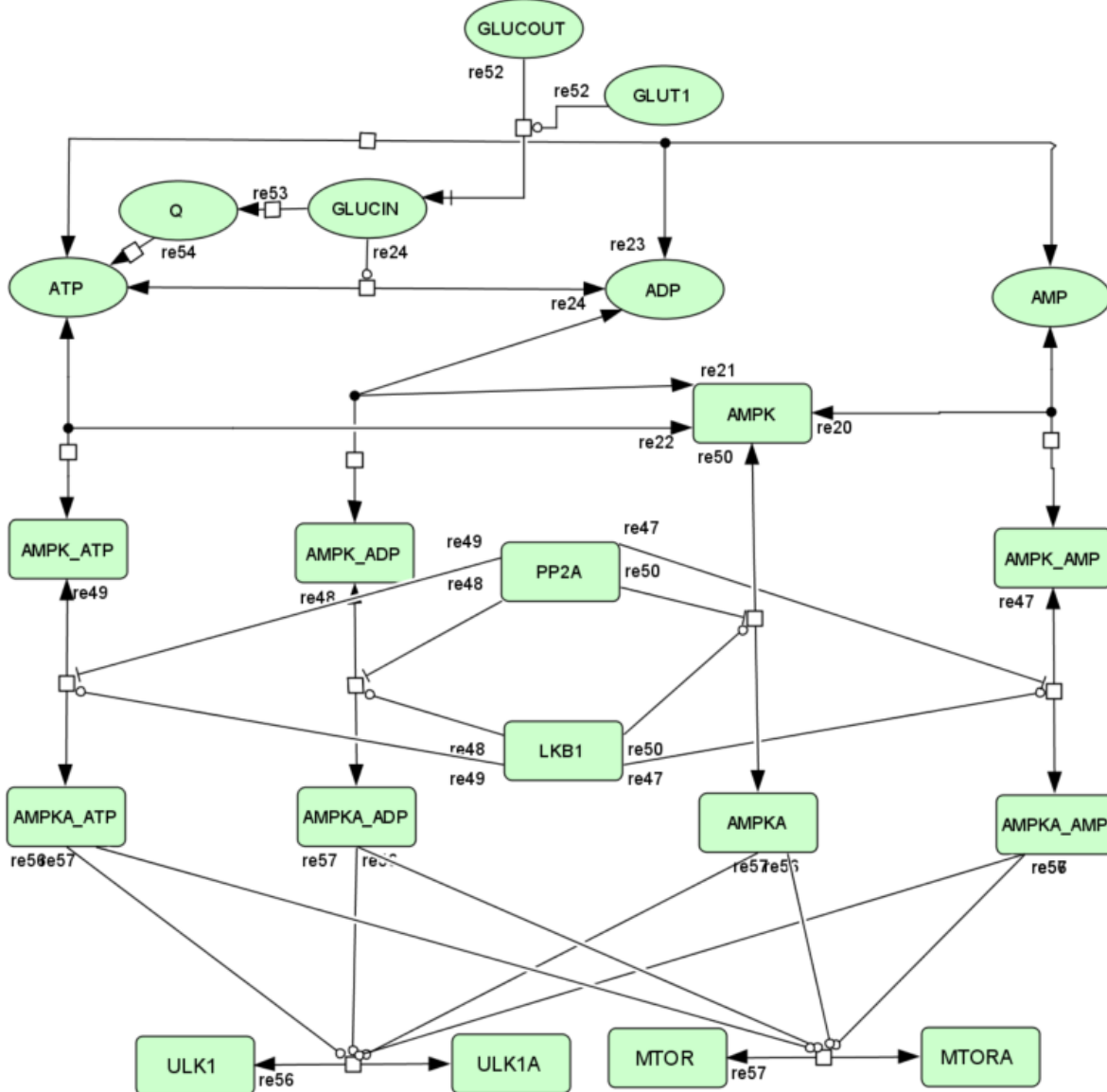


Figure 4.1: The figure illustrates the BCRN network constructed for the modeling of glucose starvation. Extracellular glucose is imported via **GLUT1** and metabolised to sustain ATP production. The produced ATP is then metabolized and is converted into ADP during glycolysis. ATP production is supported by an increase in the proton motive force (**Q**), while ATP turnover continuously produces ADP and AMP. The adenine nucleotides interconvert through both direct consumption ($\text{ATP} \rightarrow \text{ADP}$) and an AXP cycling reaction ($2 \text{ ADP} \leftrightarrow \text{ATP} + \text{AMP}$). Changes in these nucleotide concentrations drive the formation of distinct AMPK complexes (**AMPK_ATP**, **AMPK_ADP**, **AMPK_AMP**) from the unbound form (**AMPK**). AMPK activation - denoted by the letter A - is represented through phosphorylation by **LKB1**, whereas **PP2A** mediates dephosphorylation. In this submodule, all phosphorylated AMPK species are considered active regardless of their bound nucleotide. Importantly, however, the phosphorylation rates are higher for AMP and ADP bound AMPK, than for the ATP bound complexes allowing the cellular energy state to be expressed through the relative ATP/ADP/AMP levels via AMPK activation. Further downstream, active AMPK complexes (**AMPK_ATP**, **AMPK_ADP**, or **AMPK_AMP**) promote the activation of **ULK1** (**ULK1A**) and inhibit the active form of **MTOR** (**MTORA**). However, **MTORA** also inhibits AMPK, and **ULK1** provides an additional negative feedback on AMPK activity as well. Together, these loops create a closed regulatory structure that determines how the cell interprets a drop in glucose availability. For clarity, the upstream AKT-TSC-RHEB signalling branch controlling MTOR activation is omitted from this schematic but is included in the full BCRN wiring diagram provided at the *Online Supplementary Material*.

In our model, AMPK creates the connection between glucose availability and autophagy initiation by modulating MTOR and ULK1. Active AMPK enhances ULK1 activation and inhibits the active form of MTOR (MTORA). However, MTORA inhibits AMPK too, and ULK1 establishes a negative feedback loop on AMPK as well. MTORA also integrates signals from several upstream regulators not shown in this submodule: MTOR activation requires RHEBA, which is inhibited by TSCA and TSCA is inhibited by AKTA. This branch ultimately converges back onto AMPK, as active AMPK (AMPKA) attenuates AKTA-mediated inhibition of TSCA, thereby closing the regulatory loop.

The newly implemented part of the BCRN described above is depicted in Fig. 4.1. Species and interactions belonging to the AKT–TSC–RHEB axis (AKT, AKTA, TSC, TSCA, RHEB, RHEBA) are omitted here for clarity but appear in the full wiring diagram provided at the *Online Supplementary Material*.

4.2. Statistical Analysis of Basal State Model Behaviour

4.2.1 Effectiveness of the Initial Condition Sampling Strategy

The first step of our analysis examined the performance of the initial-condition sampling strategy. In our previous work (see the *Online Supplementary Material*) we derived a robust method for generating physiologically plausible initial conditions and defined an accompanying performance metric. Using this approach, the present model achieved an effectiveness of

$$eff\% = \frac{19821}{20000} \cdot 100\% = 99.1\%$$

indicating that the vast majority of sampled initial conditions led to stable and valid basal-state simulations.

4.2.2 Analysis of Covariance Convergence

To assess whether the covariance structure of the model outputs stabilizes with increasing sample size, we computed pairwise distances between covariance matrices estimated from different numbers of XML outputs (details in Section 3.2.3.2). The AIRM distances decreased consistently as N_{cond} increased, indicating convergence of the covariance estimates. For example, the distance between $\text{cov}_{(9821)}$ and $\text{cov}_{(5500)}$ was 2.8, while the comparison between $\text{cov}_{(9821)}$ and $\text{cov}_{(3000)}$ yielded a similarly low value of 5.5. In contrast, the comparison with $\text{cov}_{(50)}$ produced a larger distance of 24. Results of the KL divergence metric show a similar tendency of convergence. Here we note that the instability of this approach (at e.g., $d_{9821-502}^{\text{KL}} = 1.6 \cdot 10^3$) arises at low

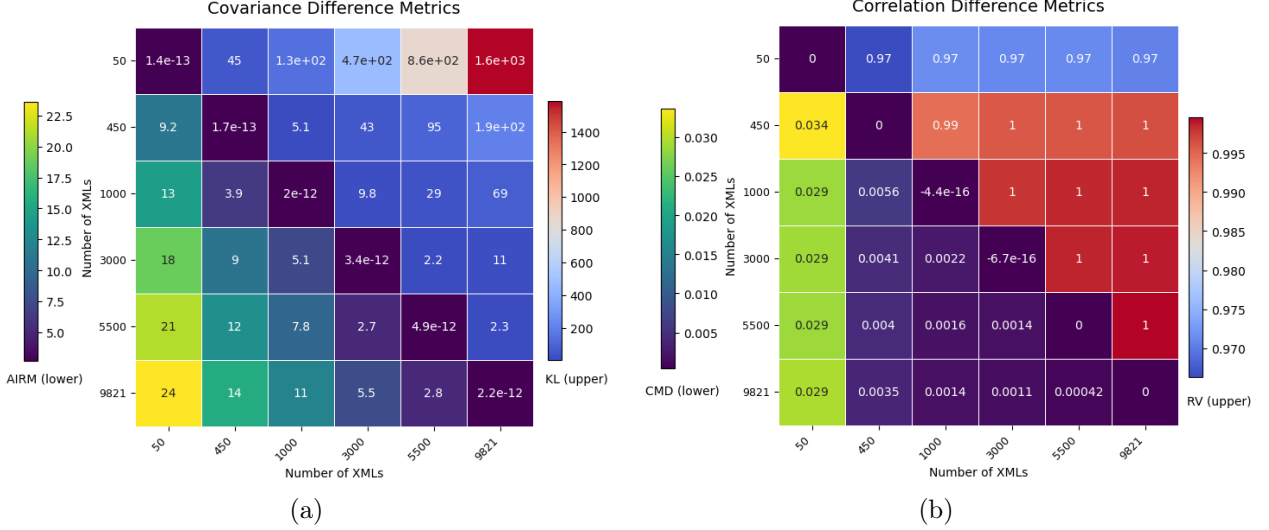


Figure 4.2: Heatmaps of pairwise distances between covariance and correlation matrices (denoted as **cov**, **corr**, respectively) estimated from increasing numbers of XML inputs. Both subfigures display the computed distances for two separate metrics to ensure a more robust result. Panel (a) shows the Affine-Invariant Riemannian Metric (AIRM) distances in the lower triangle and Kullback-Leibler (KL) divergences in the upper one quantified between covariance matrices. Panel (b) displays Correlation Matrix Distance (CMD) values in the bottom and Rho-vector (RV) *similarities* in the top, evaluated between correlation matrices. In both subfigures, the axes indicate N_{cond} , i.e., the number of model outputs used to compute each matrix. In the bottom triangle, yellow colors indicate high, while blue/purple colors indicate low values. Similarly, in the top triangle, red colors mark high values, while blue colors signal low numbers. Each block corresponds to the difference between two matrices estimated from different sample sizes. For example, the block at $x = 3000$ and $y = 9821$ in panel (a) reflects the AIRM metric between $\mathbf{cov}_{(3000)}$ and $\mathbf{cov}_{(9821)}$, while the value at $x = 9821$ and $y = 3000$ in panel (b) shows the similarity (the closer this is to one the less different the matrices are) between \mathbf{corr}_{9821} and \mathbf{corr}_{3000} . For both **cov** and **corr**, differences decrease as N_{cond} increases, indicating convergence of the covariance and correlation structures. Convergence of the covariance matrix demonstrates that the model produces a stable basal-state distribution under small perturbations of its initial conditions, while convergence of the correlation matrix enables reliable interpretation of the correlation patterns computed from the full dataset.

N_{cond} numbers occurs because the central limit theorem does not hold for low N_{cond} and thus normality cannot be assumed.

4.2.3 Analysis of Correlation Convergence

Correlation matrix distances displayed a similar convergence pattern. Using the CMD metric, we observed that distances between correlation matrices decreased as N_{cond} increased. The CMD distance between \mathbf{corr}_{9821} and $\mathbf{corr}_{(5500)}$ was 0.00042, while the comparison between $\mathbf{corr}_{(9821)}$ and $\mathbf{corr}_{(3000)}$ yielded 0.0011. As expected, matrices computed from very small samples differed more substantially: the comparison with $\mathbf{corr}_{(50)}$ gave a distance of 0.029. The computed RV similarities indicate high similarity for even low N_{cond} values, suggesting that the structure of

the correlations are similar even for small N_{cond} numbers. Values for both CMD and RV indicate that the correlation structure stabilizes with increasing sample size. The full correlation-distance heatmap is shown in Fig. 4.2b.

4.3. Simulation of Glucose Consumption

To begin, we evaluated the performance of the glucose submodule by comparing model outputs to quantitative time-course data reported by Shin et al. [45]. Figure 4.3 shows the trajectories of extracellular glucose (GLUCOUT) from $t = 0$ to $t = 84$ hours for $N = 100$ simulations, each initiated from one of 100 randomly sampled initial conditions. The initial concentration of GLUCOUT was set to 1 mM (given as $10^{-6} \frac{\text{mol}}{\text{cm}^3}$ in Fig. 4.3) for all simulations. The orange curve represents the mean trajectory across simulations, while the lighter, semi-transparent curves correspond to individual runs. Experimental measurements and their standard deviations are plotted as red error bars. Data are available every 12 hours over a 60-hour period and reflect glucose concentrations measured directly in the cell culture medium.

To quantify the accuracy of the simulations, we calculated both the squared error (SE) and the root-mean-squared error (RMSE). Agreement between model predictions and experimental measurements is excellent, with $\text{SE} = 3.21 \cdot 10^{-14}$ and $\text{RMSE} = 7.32 \cdot 10^{-8}$. The qualitative behaviour of the system is also captured correctly, as both the model and the experimental data exhibit a characteristic exponential-decay profile of extracellular glucose under starvation.

4.4. Simulation of ATP Production and Consumption

A total of $N = 200$ simulations were performed to model the time-course of ATP, ADP, and AMP concentrations from $t = 0$ to $t = 84$ hours, based on $N_{\text{cond}} = 200$ distinct initial conditions. Of these, 100 simulations represent the basal state, while the remaining 100 simulate nutrient starvation, with extracellular glucose concentrations (GLUCOUT) set to 6 mM and 1 mM, or equivalently $6 \cdot 10^{-6} \text{ mol/cm}^3$ and 10^{-6} mol/cm^3 , respectively. The dynamics under these conditions are visualized in Figure 4.4a and Figure 4.4b.

In both figures, mean concentration profiles are shown for ATP (blue), ADP (orange), and AMP (green), with all 100 corresponding simulation trajectories rendered in lighter shades of the same color. The red dotted line indicates the total concentration of the AXP pool. An extended shaded area surrounding the mean curves illustrates the interquartile range (IQR) across simulations.

The model captures canonical AXP dynamics with physiologically consistent behaviour. In

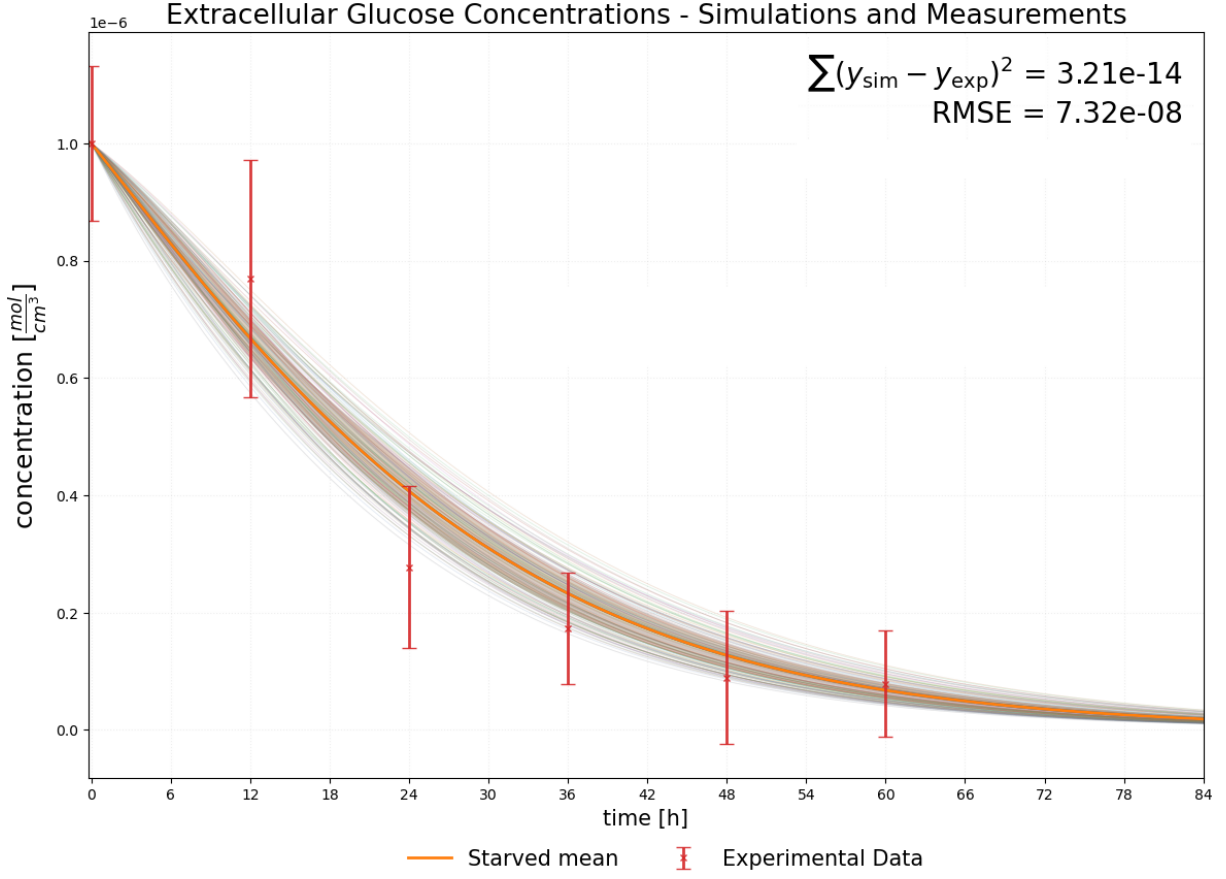


Figure 4.3: Time-course simulation trajectories and measurement data of extracellular glucose (GLUCOUT) under starvation conditions are displayed. The light grey curves correspond to 100 individual simulations generated from 100 randomly sampled initial conditions, all starting from an initial GLUCOUT concentration of $10^{-6} \frac{\text{mol}}{\text{cm}^3} = 1$ [mM]. The vertical axis shows glucose concentrations, while the horizontal axis depicts time from $t = 0$ to $t = 60$ or $t = 84$ hours for the simulations and measurements, respectively. The orange curve shows the mean trajectory across simulations. Experimental measurements from Shin et al. [45], together with their standard deviations, are shown as red error bars at 12-hour intervals. The model reproduces both the quantitative values and the characteristic exponential decay profile observed experimentally, with very low SE ($3.21 \cdot 10^{-14}$) and RMSE ($7.32 \cdot 10^{-8}$) values.

the basal state, ATP dominates the AXP pool as high extracellular glucose ensures sustained intracellular ATP production. As expected, the system remains near equilibrium, with concentrations fluctuating only slightly around steady-state values.

Under starvation, however, the system exhibits distinct phases. Initially, ATP declines rapidly while ADP and AMP rise at roughly equal rates. This is followed by a plateau phase in which concentrations remain relatively stable, suggesting that the ATP concentration drop is temporarily compensated via the ATP–ADP–AMP cycle ($\text{ATP} \rightarrow \text{ADP}$ and $2 \text{ ADP} \leftrightarrow \text{ATP} + \text{AMP}$). As glucose availability drops below a critical threshold, however, ATP begins to decrease again, while AMP continues to accumulate.

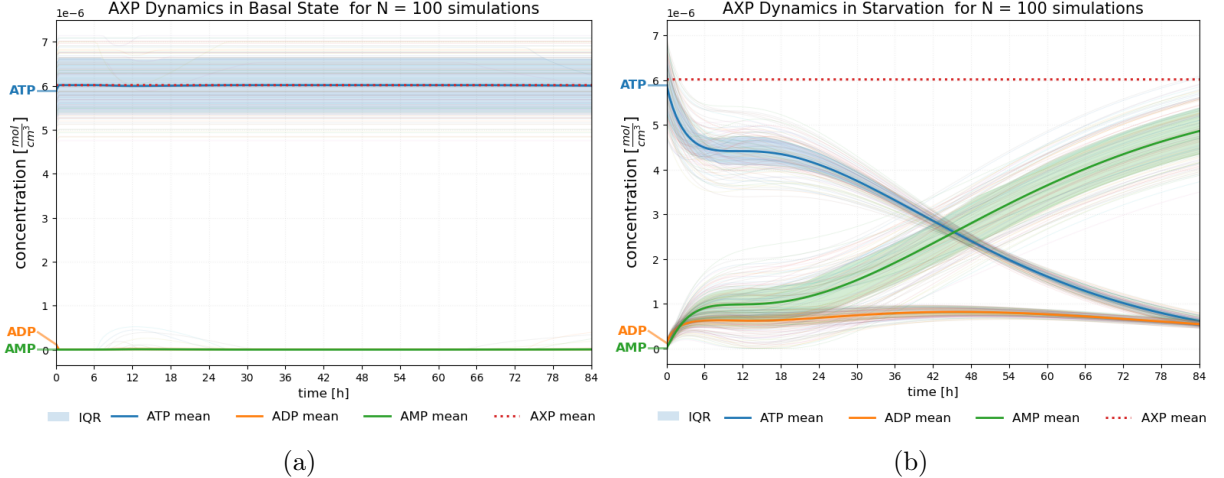


Figure 4.4: Simulated time-course profiles of ATP, ADP, and AMP concentrations under basal and glucose-starved conditions over an 84-hour period. Each trajectory corresponds to one of 100 independent simulations. Mean concentrations are shown with solid lines (ATP: blue, ADP: orange, AMP: green), surrounded by shaded areas indicating interquartile ranges. The red dotted line marks the total AXP pool. Under basal conditions, the dynamics are flat and ATP remains dominant, while ADP and AMP levels are orders of magnitudes smaller. Starvation, however, induces a multi-phased response that begins with a rapid ATP decline followed by AMP accumulation. This behaviour is consistent with experimentally measured behaviour in metabolically sensitive cell types. [104], [105], [106]

4.5. Autophagy Regulation During Starvation

As detailed in section 4.1, we constructed a model that differentiates between AMPK complexes not only based on their activity, but also based on the AXP molecule that they are bound to. Therefore, before investigating overall AMPK dynamics, we explored how AMPK is regulated by AXP concentrations

4.5.1 AMPK-AXP Dynamics

For the investigation of AMPK-AXP time profiles, we again, carried out a total of $N = 200$ simulations between $t = 0$ and $t = 84$ hours, using $N_{\text{cond}} = 200$ independently sampled initial conditions. Half of these simulations correspond to basal conditions, whereas the other half represent nutrient-starved cells. In the former case, the extracellular glucose level (GLUCOUT) was set to $6 \text{ [mM]} (= 6 \times 10^{-6} \text{ mol/cm}^3)$, while in the latter, GLUCOUT concentrations at $t = 0$ were set to $1 \text{ [mM]} (= 1 \times 10^{-6} \text{ mol/cm}^3)$. The resulting trajectories, mean curves and IQR are shown for both the basal and starvation scenarios in Figure 4.5a and Figure 4.5b. For conciseness, the legend is omitted, but the different species are connected to the curves that represent their time profiles.

All simulations were initialized with active AMPK complexes at $10^{-14} \text{ mol/cm}^3$ and inactive

forms at 10^{-10} mol/cm³, reflecting a presumed homeostatic state at $t = 0$. In the basal setting, the system rapidly stabilizes after $t > 0$, with minimal change across all AMPK–AXP complexes. The dominant species remains AMPK_ATP (purple curve), which is consistent with its role as the ATP-bound, inactive conformation under energy-rich conditions [52], [53], [92]. The stability of the trajectories further supports the model’s appropriate baseline behaviour. The dominant complex of the pool in this scenario is AMPK_ATP (brown curve), which reflects the biological function of active AMPK as being the sensor of nutrient stress that is mediated by elevated AMP:ATP and ADP:ATP ratios [51], [53], [92].

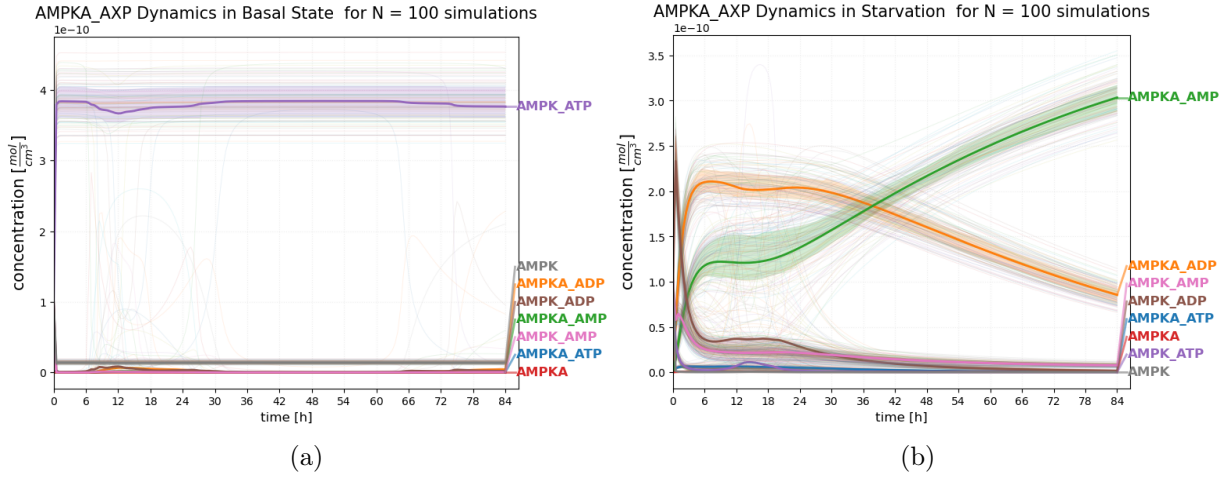


Figure 4.5: The figure shows time-course dynamics of AMPK–AXP complexes under basal and glucose-starved conditions, based on $N = 100$ simulations per condition. Mean curves from $t=0$ to $t=84$ hours are shown for each AMPK complex: AMPK_ATP (blue), AMPK_ATD (orange), AMPK_AP (green), AMPK_ATP (purple), AMPK_DAD (brown), AMPK_DAP (pink), AMPK (gray). Shaded areas represent the interquartile range (IQR). Under basal conditions (Fig. 4.5a), the system remains stable with AMPK_ATP as the dominant form. Under starvation in Fig. 4.5b, however, the AMPK pool shifts from inactive forms toward active species, with a gradual transition from AMPK_ATD to AMPK_AP dominance.

4.5.2 Dynamics of the mTORC1-ULK1/2-AMPK Regulatory Triangle

Following the exploration of AMPK-AXP dynamics, we next analyzed the behaviour of the mTORC1–ULK1/2–AMPK signaling axis under basal and glucose-starved conditions. Figures 4.6a and 4.6b show simulation results for both conditions. In total, $N = 200$ simulations were conducted, with $N_{\text{cond}} = 100$ simulations corresponding to each state. The extracellular glucose concentration (GLUCOUT) was initialized at $6 \cdot 10^{-6}$ mol/cm³ for the basal state, and at $1 \cdot 10^{-6}$ mol/cm³ for the starvation condition. Simulations were run from $t = 0$ to $t = 84$ hours.

The six variables tracked are: total inactive AMPK (AMPK_t), total active AMPK (AMPKA_t),

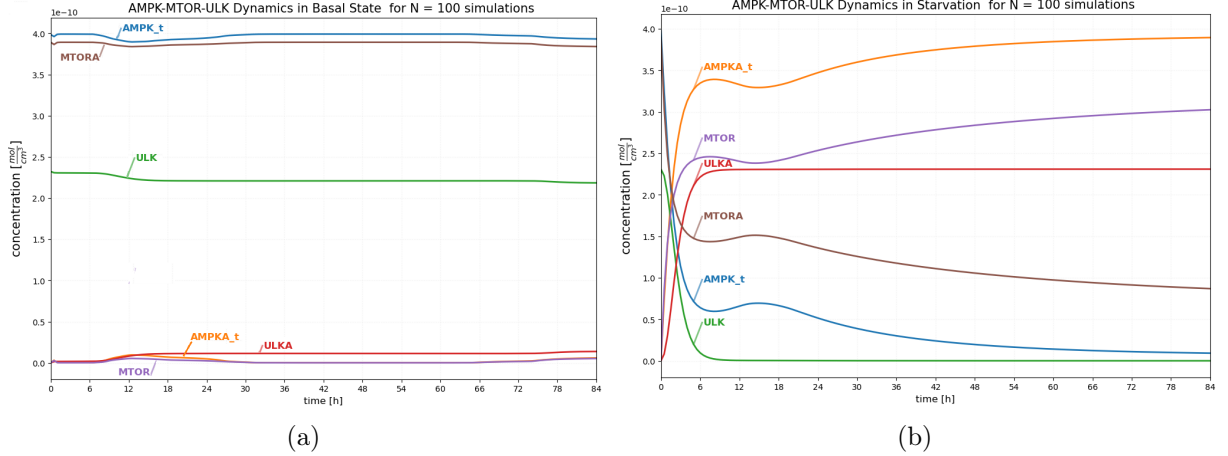


Figure 4.6: Time-course simulation of six key species in the AMPK–mTORC1–ULK1/2 network under basal and glucose-starved conditions. Each curve shows the mean concentration over $N = 100$ simulations per condition. Species include inactive AMPK (AMPK_t, blue), active AMPK (AMPKA_t, orange), inactive mTORC1 (MTOR, purple), active mTORC1 (MTORA, brown), inactive ULK1/2 (ULK, green), and active ULK1/2 (ULKA, red). Under basal conditions, AMPKA_t and ULKA remain low while MTORA dominates. Under starvation, AMPKA_t and ULKA increase while MTORA is inhibited, consistent with autophagy induction via AMPK signaling.

inactive mTORC1 (MTOR), active mTORC1 (MTORA), inactive ULK1/2 (ULK), and active ULK1/2 (ULKA). AMPK_t is defined as the sum of all inactive AMPK complexes: AMPK, AMPK_ATP, AMPK_ADP, and AMPK_AMP. Similarly, AMPKA_t aggregates the active complexes AMPKA, AMPKA_ATP, AMPKA_ADP, and AMPKA_AMP.

Under basal conditions (Figure 4.6a), the system quickly reaches a steady state. Active complexes AMPKA_t (orange) and ULKA (red) remain at or near their initial concentrations (approximately 10^{-14} mol/cm³), along with the inactive complex, MTOR (purple). In contrast, the inactive complexes, AMPK_t (blue) and ULK (green) as well as the active complex, MTORA (brown) show significantly higher concentrations. This behaviour accurately reflects the quiescent autophagy under physiologic conditions.

In contrast, the starvation condition (Figure 4.6b) produces dynamic changes. Levels of AMPKA_t rise steadily after a steep initial incline and before plateauing. As AMPKA_t increases, its downstream target ULKA is activated, while MTORA concentrations fall sharply - from around $5 \cdot 10^{-10}$ to approximately $1 \cdot 10^{-10}$ mol/cm³. Conversely, MTOR levels rise, and both AMPK_t and ULK concentrations decline.

Chapter 5

Discussion

5.1. Representing Accurate AMPK-AXP Dynamics in Glucose Starvation

In our model, we explicitly represent different forms of AMPK depending on which adenine nucleotide (ATP, ADP, or AMP) is bound to its regulatory sites. This mechanistic detail allows the model to more accurately capture the relationship between AMPK activation dynamics and the cellular energy state.

Catalytic activity is shown by AMPK when it is phosphorylated at Thr 172 [51], [52]. ATP-bound AMPK is therefore, generally inactive as ATP promotes dephosphorylation, whereas binding of AMP or ADP promotes AMPK activation by phosphorylation at Thr172 [51], [92]. Crucially, however, AMP binding triggers allosteric activation as well and thus further enhances AMPK’s activity levels, while ADP binding simply protects AMPK from dephosphorylation. Our BCRN model accounts for these differences by treating ATP-, ADP-, and AMP-bound AMPK as separate species in the reaction network. As a result, the modeled AMPK dynamics align closely with AXP levels and thus represent energy status reliably. Overall, the model captures semi-quantitative behaviour as demonstrated by Fig. 4.4 and 4.5 [50]. Additionally, fully quantitative reproduction of experimental behaviour remains unrealistic, as measurements for network optimization are scarce and protein-level dynamics vary substantially between individual cells [107], [108].

5.2. Consequences of Effective IC Sampling and Convergence

The model we developed is intentionally compact and simple and relies predominantly on literature-derived rate constants and initial conditions. This design choice results in a system whose

basal-state behaviour is not dominated by free parameters but instead reflects experimentally motivated kinetics. To ensure that this behaviour is robust, we evaluated the model under large sets of randomly sampled initial conditions.

The high sampling effectiveness and the convergence of both covariance and correlation matrices demonstrate that the network reliably stabilizes into a stationary basal state. In practice, this means that small perturbations of the initial conditions do not lead to qualitatively different steady-state behaviours, which is essential for a model intended to simulate starvation-induced deviations from homeostasis.

We also note here that the sampling and the consequent evaluation had to occur in terms of concentrations remaining in a relatively wide range which may have influenced our high *eff%* score. The reason for this is that cellular protein concentrations are generally not well-known due to high cell-to-cell variability and noisy measurements [109]. Even within uniform cell populations, protein abundance often varies by orders of magnitude, and quantifying these differences reliably is challenging [110]. Regardless however, the results of the statistical analysis reveal that in basal state, our model’s proteins remain in biologically valid ranges. Therefore, with this stability established, we proceeded to study glucose-starvation scenarios. We evaluated the biological plausibility of the predictions at four levels: glucose handling, AXP dynamics, AMPK–AXP behaviour, and the downstream regulation mediated through the AMPK-mTORC1–ULK1/2 axis.

5.3. Information Flow in Our Minimal Model and in More Inclusive Ones

5.3.1 Propagation of Starvation Signal Throughout Distinct Submodules

Figure 4.3 demonstrates that the model accurately reproduces the experimentally measured decline of extracellular glucose under starvation. This agreement is crucial, as the dynamics of extracellular glucose depletion constitute the first step of the information flow from nutrient levels to intracellular sensing, AXP pool rebalancing, and ultimately AMPK-driven autophagy initiation.

According to the experimental observations in both transformed and non-transformed cells under starvation, after the initial dip in ATP concentrations, the ATP-ADP-AMP cycle may rescue cellular ATP levels [111] leading to a short relatively flat period which is followed by the continued decay of ATP concentrations as the $\text{ATP} \rightarrow \text{ADP}$ and $2 \text{ ADP} \leftrightarrow \text{ATP} + \text{AMP}$ reactions inevitably begin to shift towards elevating AMP concentrations in the absence of an extracellular glucose source [104], [105], [106]. In Fig. 4.4b we accurately recreate not only

general AXP dynamics during starvation [91], [92], [107], but also the multiphasic structure of glucose-deprivation-triggered AXP dynamics: between approximately $t = 6$ and $t = 18$ h, cellular ATP levels temporarily plateau after the initial dip before continuing to decrease.

The explicit modelling of the three AMPK–AXP complexes reveals two biologically meaningful behaviours. First, we recover previous findings that ADP is the primary activator of AMPK in mildly starved or near-physiological conditions, with AMP-driven activation becoming more prominent only as starvation persists and AMP levels rise [52], [53], [92]. This is reflected in Figure 4.5b, where AMPK_{ADP} rises before AMPKA_{AMP}, consistent with Coccimiglio et al.’s model [92]. Second, because our network tracks each binding state separately, the AMPK activation profile mirrors the richer AXP behaviour rather than collapsing it into a single AMP/ATP ratio. Thus, the AMPK module inherits and preserves the detailed structure of the AXP module (compare Fig. 4.4 with Fig. 4.5), confirming that energy stress signals are propagated faithfully.

At the higher regulatory level, we expect that in basal conditions mTORC1 is active (i.e., MTORA levels are high) and this promotes anabolic processes by inhibiting the active AMPK complexes (AMPKA) and the autophagy inducing protein complex ULK1/2 (ULKA in the model). In contrast, under starvation, AMPK should be activated (i.e., we expect high AMPKA) which should in turn activate ULK1/2 and inhibit mTORC1 [25], [26]. Based on Figures 4.5a and 4.5b, we conclude that the AMPK–mTORC1–ULK1/2 regulatory triangle displays this expected switch between basal and starvation-induced states: elevated MTORA and low ULKA and AMPKA levels in nutrient-rich conditions, and high AMPKA and ULKA with suppressed MTORA during starvation.

Additionally, we note that an interesting peak highlighting information flow between submodules can be observed in the total inactive AMPK levels, AMPK_t, as well as in the active AMPKA_t, MTOR, and MTORA levels: around $t = 16$ h, active AMPKA concentrations drop and inactive AMPK concentrations rise for a short while. This is also reflected at this time by a short increase in active mTORC1 concentrations and decrease in inactive mTORC1 concentrations. The timing of these dips mirrors the transient ATP plateau and suggests that the AMPK-mTORC1-ULK1/2 modules experience and transmit the same temporary rescue of declining ATP concentrations mentioned above and highlighted by Fig. 4.4b.

Together, these patterns illustrate that our model does not simply reproduce isolated reactions, but captures the coordinated transmission of energy stress signals across molecular layers. This provides the foundation for situating our findings within the broader context of cellular information processing.

5.4. Current Limitations and Future Directions

5.4.1 Limitations

Although, qualitative agreement between our simulation results and published studies is strong [51], [91], [92], [112] allowing us to conclude that our model faithfully reproduces glucose, AXP, AMPK-AXP, as well as AMPK-mTORC1-ULK1/2 dynamics under both nutrient-rich and starved conditions, we must note that in the absence of direct time-resolved experimental measurements, the model remains semi-quantitative and cannot represent exact quantitative dynamics.

This leads us to the primary limitation of our model which is that it lacks rigorous experimental validation of the simulated time courses (except for glucose consumption). This is because obtaining experimental data measuring protein concentrations over time under various stress signals has proven to be exceptionally difficult [113], [114], [115]. Biological experiments are typically more concerned with qualitative properties of the system (such as direction and relative magnitude of change) than with quantitative, time-resolved concentration profiles [115], [116]. Additionally, most protein concentration time profiles are measured by Western blots, which are semi-quantitative and susceptible to technical variability and noise [109], [117], [118]. This is due to the high cell-to-cell variability as well as due to the complex, multi-step measurement process of western blot analysis. As a result, cross-validation of simulated and experimental trajectories is often restricted to a qualitative comparison for most modules of our model and for BCRNs in general [119], [120].

As a consequence of scarce data availability, another typical limitation of biochemical reaction network models is that the optimization of rate parameters by experimental data is numerically difficult [83], [85], [86]. The low time resolution and noisy time-course measurements, usually created with the experimental goal of gaining qualitative and not quantitative insights into a process, make it challenging to perform mathematically rigorous parameter estimations to obtain the generally unknown and perhaps not even time- and temperature-invariant rate parameters governing the BCRN models [85], [87], [88]. Our model, however, mostly overcomes this limitation by using rate constants derived from a rigorous literature review conducted before simulations began.

The difficulty of insufficient parameter data is further exacerbated by the interconnectedness of biochemical regulatory pathways. Simplifying these networks may ease parameter estimation but it risks removing essential biology and producing unrealistic computational behaviour. As discussed in section 1, the real regulatory landscape of autophagy is considerably more intricate

than reflected in this minimal network of 44 species. Regulatory cues from apoptosis, energy metabolism, calcium signaling, and inositol pathways also shape autophagy [4], [71]. This, however, is a limitation of the model that we are actively working to mitigate as our long-term goal is the implementation of a holistic BCRN describing the full autophagy–apoptosis decision process.

5.4.2 Future Directions and Applications

Despite the limitations of our model, implementing the correct flow of stress signals from glucose through AXPs and AMPK toward mTORC1 and ULK1/2 is a foundational step toward the long-term objective of our research group to implement a large-scale model of autophagy–apoptosis crosstalk under different stress conditions [81].

This large-scale BCRN model currently consists of five interconnected submodules encompassing calcium, inositol, mTOR, apoptosis, and autophagy signaling. Each module includes key regulatory proteins such as AMPK for autophagy, calpain for calcium, and p53 for apoptosis [81]. This work extends the autophagy and mTOR submodules, enabling the simulation of glucose starvation which is one of the major stressors used in autophagy induction [121], [122].

The integration of these modules not only enhances the mechanistic realism of our model but also opens the door to personalized simulations of cellular behavior. With accurate measurements of the initial protein concentrations, the model can be adapted to reflect individual cellular conditions. Using this framework, we can simulate how different pathologies involving autophagy–apoptosis crosstalk and their potential treatments, affect key regulatory molecules over time. This approach holds significant promise for advancing precision medicine by helping to predict patient-specific responses and minimizing adverse side effects [83].

The broader relevance of this work lies in its potential to connect computational systems biology and biomedical research. As recent studies increasingly highlight the central role of autophagy and apoptosis in both physiological and pathological contexts [8], their complex interdependence continues to hinder their experimental disentanglement and therapeutic exploitation [79]. Importantly, emerging research also highlights the pivotal role of autophagy in ageing biology, where shifts in mTOR and AMPK activity appear to influence the recycling of damaged cellular components and thereby modulate age-associated physiological decline [123], [124], [125]. Suppressed autophagic activity is increasingly associated with neurodegeneration, cancer, and other pathologies that become more prevalent in elderly individuals [6], [7], [126], further highlighting the need for accurate mechanistic models of autophagy. For all these reasons, in aging western societies primary emphasis should be placed on the enhancement of our understanding

of autophagy. By offering an integrative perspective on autophagy-apoptosis interactions, our model ultimately aims to contribute to a deeper understanding of the etiology and progression of diseases linked to autophagy or apoptosis dysfunction, such as Alzheimer’s disease, cancer, and chronic inflammation [9], [127], [128]. Ultimately, such systems-level frameworks may support the development of more targeted and effective therapeutic strategies, enabling medical professionals to create digital twins of patient-specific cellular states to guide personalized treatments [129], [130], [131].

Chapter 6

Summary

This thesis addresses how extracellular glucose starvation influences the activation of autophagy through AMPK. The work builds on a previously published biochemical reaction network (BCRN) describing autophagy–apoptosis regulation under basal conditions. The primary goal was to extend this model by implementing a glucose starvation module that links energy stress to autophagy induction through realistic, systems-level dynamics. The extended model now includes glucose uptake, ATP production and consumption, AXP (ATP, ADP, AMP) dynamics, and AMPK activation. Importantly, it distinguishes between nucleotide-bound forms of AMPK and captures its activation in a biologically consistent manner.

All four core objectives of the thesis were successfully achieved. First, a biologically grounded wiring diagram was constructed and integrated into the existing BCRN framework with physiological initial conditions and parameters derived from the literature. Second, the model’s stability and robustness were tested under basal conditions using statistical analysis of thousands of simulations. Third, simulations under starvation were conducted and these accurately reproduced key features observed in experimental data, such as the transient plateau of ATP levels, nucleotide level dependent AMPK activation, and the subsequent downstream modulation of mTORC1 and ULK1/2 activity. Finally, the model’s accuracy in representing the biological propagation of the starvation signal was discussed.

Overall, the model provides a coherent picture of how metabolic stress signals propagate from glucose availability through AXP levels to AMPK, ultimately leading to autophagy initiation. These results offer an essential foundation for future model extensions. Specifically, the implementation of glucose starvation as a modular and biologically consistent input prepares the ground for integrating this pathway into a larger BCRN model that aims to capture autophagy–apoptosis crosstalk under multiple types of cellular stresses.

In the long term, this research supports the broader goal of simulating cell-fate decisions in a

physiologically meaningful way. The model could potentially be adapted for predictive, patient-specific simulations by incorporating experimentally measured protein concentrations. Such a tool may prove valuable in biomedical research and personalized medicine by informing therapeutic strategies and identifying key regulators of disease-related pathways involving autophagy and apoptosis.

Bibliography

- [1] V. Ruprecht et al., “How cells respond to environmental cues—insights from bio-functionalized substrates,” *Journal of cell science*, vol. 130, no. 1, pp. 51–61, 2017. DOI: doi.org/10.1242/jcs.196162.
- [2] M. F. Ullo and L. B. Case, “How cells sense and integrate information from different sources,” *WIREs Mechanisms of Disease*, vol. 15, no. 4, e1604, 2023. DOI: [10.1002/wsbm.1604](https://doi.org/10.1002/wsbm.1604).
- [3] M. Casdagli, “A dynamical systems approach to modeling input-output systems,” in *SANTA FE INSTITUTE STUDIES IN THE SCIENCES OF COMPLEXITY-PROCEEDINGS VOLUME-*, Addison-Wesley Publishing Co, vol. 12, 1992, pp. 265–265.
- [4] B. Liu et al., “Quantitative assessment of cell fate decision between autophagy and apoptosis,” *Scientific reports*, vol. 7, no. 1, p. 17605, 2017. DOI: [10.1038/s41598-017-18001-w](https://doi.org/10.1038/s41598-017-18001-w).
- [5] S. Shen, Y. Shao, and C. Li, “Different types of cell death and their shift in shaping disease,” *Cell death discovery*, vol. 9, no. 1, p. 284, 2023. DOI: [10.1038/s41420-023-01581-0](https://doi.org/10.1038/s41420-023-01581-0).
- [6] Y. Aman et al., “Autophagy in healthy aging and disease,” *Nature aging*, vol. 1, no. 8, pp. 634–650, 2021. DOI: [10.1038/s43587-021-00098-4](https://doi.org/10.1038/s43587-021-00098-4).
- [7] S. Metzger et al., “Age at onset in huntington’s disease is modified by the autophagy pathway: Implication of the v471a polymorphism in atg7,” *Human genetics*, vol. 128, no. 4, pp. 453–459, 2010. DOI: [10.1007/s00439-010-0873-9](https://doi.org/10.1007/s00439-010-0873-9).
- [8] P. Jiang and N. Mizushima, “Autophagy and human diseases,” *Cell research*, vol. 24, no. 1, pp. 69–79, 2014. DOI: [10.1038/cr.2013.161](https://doi.org/10.1038/cr.2013.161).
- [9] B.-Z. Shao, Y. Yao, J.-S. Zhai, J.-H. Zhu, J.-P. Li, and K. Wu, “The role of autophagy in inflammatory bowel disease,” *Frontiers in Physiology*, vol. 12, p. 621132, 2021. DOI: [10.3389/fphys.2021.621132](https://doi.org/10.3389/fphys.2021.621132).

- [10] K. Newton, A. Strasser, N. Kayagaki, and V. M. Dixit, “Cell death,” *Cell*, vol. 187, no. 2, pp. 235–256, 2024. DOI: [10.1016/j.cell.2023.11.044](https://doi.org/10.1016/j.cell.2023.11.044).
- [11] P. Syntichaki and N. Tavernarakis, “Death by necrosis,” *EMBO reports*, 2002. DOI: [10.1093/embo-reports/kvf138](https://doi.org/10.1093/embo-reports/kvf138).
- [12] S. Kesavardhana, R. S. Malireddi, and T.-D. Kanneganti, “Caspases in cell death, inflammation, and pyroptosis,” *Annual review of immunology*, vol. 38, no. 1, pp. 567–595, 2020. DOI: [10.1146/annurev-immunol-073119-095439](https://doi.org/10.1146/annurev-immunol-073119-095439).
- [13] M. S. D’arcy, “Cell death: A review of the major forms of apoptosis, necrosis and autophagy,” *Cell biology international*, vol. 43, no. 6, pp. 582–592, 2019. DOI: [10.1002/cbin.11137](https://doi.org/10.1002/cbin.11137).
- [14] I. Tanida, “Autophagy basics,” *Microbiology and immunology*, vol. 55, no. 1, pp. 1–11, 2011. DOI: [10.1111/j.1348-0421.2010.00271.x](https://doi.org/10.1111/j.1348-0421.2010.00271.x).
- [15] G. Eskander, S. G. Abdelhamid, S. A. Wahdan, and S. M. Radwan, “Insights on the crosstalk among different cell death mechanisms,” *Cell Death Discovery*, vol. 11, no. 1, p. 56, 2025. DOI: [10.1038/s41420-025-02328-9](https://doi.org/10.1038/s41420-025-02328-9).
- [16] W. Cao, J. Li, K. Yang, and D. Cao, “An overview of autophagy: Mechanism, regulation and research progress,” *Bulletin du cancer*, vol. 108, no. 3, pp. 304–322, 2021. DOI: [10.1016/j.bulcan.2020.11.004](https://doi.org/10.1016/j.bulcan.2020.11.004).
- [17] R. F. Zaarour et al., “Role of hypoxia-mediated autophagy in tumor cell death and survival,” *Cancers*, vol. 13, no. 3, p. 533, 2021. DOI: [10.3390/cancers13030533](https://doi.org/10.3390/cancers13030533).
- [18] T. Yorimitsu and D. J. Klionsky, “Autophagy: Molecular machinery for self-eating,” *Cell Death & Differentiation*, vol. 12, no. 2, pp. 1542–1552, 2005. DOI: [10.1038/sj.cdd.4401765](https://doi.org/10.1038/sj.cdd.4401765).
- [19] S. W. Ryter, S. M. Cloonan, and A. M. Choi, “Autophagy: A critical regulator of cellular metabolism and homeostasis,” *Molecules and cells*, vol. 36, no. 1, pp. 7–16, 2013. DOI: [10.1007/s10059-013-0140-8](https://doi.org/10.1007/s10059-013-0140-8).
- [20] J. Kaur and J. Debnath, “Autophagy at the crossroads of catabolism and anabolism,” *Nature reviews Molecular cell biology*, vol. 16, no. 8, pp. 461–472, 2015. DOI: [10.1038/nrm4024](https://doi.org/10.1038/nrm4024).
- [21] X. Yang et al., “The role of autophagy induced by tumor microenvironment in different cells and stages of cancer,” *Cell & bioscience*, vol. 5, no. 1, p. 14, 2015. DOI: [10.1186/s13578-015-0005-2](https://doi.org/10.1186/s13578-015-0005-2).

- [22] N. Mizushima and M. Komatsu, “Autophagy: Renovation of cells and tissues,” *Cell*, vol. 147, no. 4, pp. 728–741, 2011. DOI: [10.1016/j.cell.2011.10.026](https://doi.org/10.1016/j.cell.2011.10.026).
- [23] A. Meléndez and T. P. Neufeld, “The cell biology of autophagy in metazoans: A developing story,” *Biologists*, 2008. DOI: [10.1242/dev.016105](https://doi.org/10.1242/dev.016105).
- [24] Y. Zhu, F. Liu, F. Jian, and Y. Rong, “Recent progresses in the late stages of autophagy,” *Cell Insight*, vol. 3, no. 2, p. 100152, 2024. DOI: [10.1016/j.cellin.2024.100152](https://doi.org/10.1016/j.cellin.2024.100152).
- [25] B. Hajdú, L. Csabai, M. Márton, M. Holczer, T. Korcsmáros, and O. Kapuy, “Oscillation of autophagy induction under cellular stress and what lies behind it, a systems biology study,” *International Journal of Molecular Sciences*, vol. 24, no. 8, p. 7671, 2023. DOI: [10.3390/ijms24087671](https://doi.org/10.3390/ijms24087671).
- [26] C. H. Jung et al., “Ulk-atg13-fip200 complexes mediate mtor signaling to the autophagy machinery,” *Molecular biology of the cell*, vol. 20, no. 7, pp. 1992–2003, 2009. DOI: [10.1091/mbc.e08-12-1249](https://doi.org/10.1091/mbc.e08-12-1249).
- [27] M. B. Menon and S. Dhamija, “Beclin 1 phosphorylation—at the center of autophagy regulation,” *Frontiers in cell and developmental biology*, vol. 6, p. 137, 2018. DOI: [10.3389/fcell.2018.00137](https://doi.org/10.3389/fcell.2018.00137).
- [28] I. Tanida, T. Ueno, and E. Kominami, “Lc3 and autophagy,” in *Autophagosome and phagosome*, Springer, 2008, pp. 77–88. DOI: [10.1007/978-1-59745-157-4_4](https://doi.org/10.1007/978-1-59745-157-4_4).
- [29] C. Trejo-Solís et al., “Autophagic and apoptotic pathways as targets for chemotherapy in glioblastoma,” *International journal of molecular sciences*, vol. 19, no. 12, p. 3773, 2018. DOI: [10.3390/ijms19123773](https://doi.org/10.3390/ijms19123773).
- [30] D. Garcia and R. J. Shaw, “Ampk: Mechanisms of cellular energy sensing and restoration of metabolic balance,” *Molecular cell*, vol. 66, no. 6, pp. 789–800, 2017. DOI: [10.1016/j.molcel.2017.05.032](https://doi.org/10.1016/j.molcel.2017.05.032).
- [31] M. Holczer, B. Hajdú, T. Lőrincz, A. Szarka, G. Bánhegyi, and O. Kapuy, “Fine-tuning of ampk–ulk1–mtorc1 regulatory triangle is crucial for autophagy oscillation,” *Scientific Reports*, vol. 10, no. 1, p. 17803, 2020. DOI: [10.1038/s41598-020-75030-8](https://doi.org/10.1038/s41598-020-75030-8).
- [32] A. R. Kristensen et al., “Ordered organelle degradation during starvation-induced autophagy,” *Molecular & cellular proteomics*, vol. 7, no. 12, pp. 2419–2428, 2008. DOI: [10.1074/mcp.M800184-MCP200](https://doi.org/10.1074/mcp.M800184-MCP200).

- [33] A. Djajadikerta, S. Keshri, M. Pavel, R. Prestil, L. Ryan, and D. C. Rubinsztein, “Autophagy induction as a therapeutic strategy for neurodegenerative diseases,” *Journal of molecular biology*, vol. 432, no. 8, pp. 2799–2821, 2020. DOI: [10.1016/j.jmb.2019.12.035](https://doi.org/10.1016/j.jmb.2019.12.035).
- [34] M. Li, J. Tan, Y. Miao, P. Lei, and Q. Zhang, “The dual role of autophagy under hypoxia-involvement of interaction between autophagy and apoptosis,” *Apoptosis*, vol. 20, no. 6, pp. 769–777, 2015. DOI: [10.1007/s10495-015-1110-8](https://doi.org/10.1007/s10495-015-1110-8).
- [35] H. Rodriguez-Rocha, A. Garcia-Garcia, M. I. Panayiotidis, and R. Franco, “Dna damage and autophagy,” *Mutation Research/Fundamental and Molecular Mechanisms of Mutagenesis*, vol. 711, no. 1-2, pp. 158–166, 2011. DOI: [10.1016/j.mrfmmm.2011.03.007](https://doi.org/10.1016/j.mrfmmm.2011.03.007).
- [36] T. Pan, P. Rawal, Y. Wu, W. Xie, J. Jankovic, and W. Le, “Rapamycin protects against rotenone-induced apoptosis through autophagy induction,” *Neuroscience*, vol. 164, no. 2, pp. 541–551, 2009. DOI: [10.1016/j.neuroscience.2009.08.014](https://doi.org/10.1016/j.neuroscience.2009.08.014).
- [37] B. Caramés, A. Hasegawa, N. Taniguchi, S. Miyaki, F. J. Blanco, and M. Lotz, “Autophagy activation by rapamycin reduces severity of experimental osteoarthritis,” *Annals of the rheumatic diseases*, vol. 71, no. 4, pp. 575–581, 2012. DOI: [10.1136/annrheumdis-2011-200557](https://doi.org/10.1136/annrheumdis-2011-200557).
- [38] Q. Sun et al., “Rapamycin inhibits activation of ampk-mtor signaling pathway-induced alzheimer’s disease lesion in hippocampus of rats with type 2 diabetes mellitus,” *International Journal of Neuroscience*, vol. 129, no. 2, pp. 179–188, 2019. DOI: [10.1080/00207454.2018.1491571](https://doi.org/10.1080/00207454.2018.1491571).
- [39] L. Shang, S. Chen, F. Du, S. Li, L. Zhao, and X. Wang, “Nutrient starvation elicits an acute autophagic response mediated by ulk1 dephosphorylation and its subsequent dissociation from ampk,” *Proceedings of the National Academy of Sciences*, vol. 108, no. 12, pp. 4788–4793, 2011. DOI: [10.1073/pnas.1100844108](https://doi.org/10.1073/pnas.1100844108).
- [40] P.-M. Wong, Y. Feng, J. Wang, R. Shi, and X. Jiang, “Regulation of autophagy by co-ordinated action of mtorc1 and protein phosphatase 2a,” *Nature communications*, vol. 6, no. 1, p. 8048, 2015. DOI: [10.1038/ncomms9048](https://doi.org/10.1038/ncomms9048).
- [41] J.-P. Decuypere et al., “Ins (1, 4, 5) p 3 receptor-mediated ca²⁺ signaling and autophagy induction are interrelated,” *Autophagy*, vol. 7, no. 12, pp. 1472–1489, 2011. DOI: [10.4161/auto.7.12.17909](https://doi.org/10.4161/auto.7.12.17909).
- [42] P. Nicklin et al., “Bidirectional transport of amino acids regulates mtor and autophagy,” *Cell*, vol. 136, no. 3, pp. 521–534, 2009. DOI: [10.1016/j.cell.2008.11.044](https://doi.org/10.1016/j.cell.2008.11.044).

- [43] Y. Zhang, S. Ren, Y. Liu, K. Gao, Z. Liu, and Z. Zhang, “Inhibition of starvation-triggered endoplasmic reticulum stress, autophagy, and apoptosis in arpe-19 cells by taurine through modulating the expression of calpain-1 and calpain-2,” *International Journal of Molecular Sciences*, vol. 18, no. 10, p. 2146, 2017. DOI: [10.3390/ijms18102146](https://doi.org/10.3390/ijms18102146).
- [44] G. I. Bell et al., “Molecular biology of mammalian glucose transporters,” *Diabetes care*, vol. 13, no. 3, pp. 198–208, 1990. DOI: [10.2337/diacare.13.3.198](https://doi.org/10.2337/diacare.13.3.198).
- [45] S. Shin et al., “Erk2 mediates metabolic stress response to regulate cell fate,” *Molecular cell*, vol. 59, no. 3, pp. 382–398, 2015. DOI: [10.1016/j.molcel.2015.06.020](https://doi.org/10.1016/j.molcel.2015.06.020).
- [46] M. Leventić, K. Mišković Špoljarić, K. Vojvodić, N. Kovačević, M. Obradović, and T. Opačak-Bernardi, “The response of cell cultures to nutrient-and serum-induced changes in the medium,” *Sci*, vol. 7, no. 3, p. 105, 2025. DOI: [10.3390/sci7030105](https://doi.org/10.3390/sci7030105).
- [47] G. M. Dunn J, “Physiology, adenosine triphosphate.,” *StatPearls Publishing*, vol. StatPearls [Internet], 2025. [Online]. Available: https://www.ncbi.nlm.nih.gov/books/NBK553175/?utm_source=chatgpt.com.
- [48] H. Huang et al., “Physiological levels of atp negatively regulate proteasome function,” *Cell research*, vol. 20, no. 12, pp. 1372–1385, 2010. DOI: [10.1038/cr.2010.123](https://doi.org/10.1038/cr.2010.123).
- [49] J. Dong and M. Zhao, “In-vivo fluorescence imaging of adenosine 5-triphosphate,” *TrAC Trends in Analytical Chemistry*, vol. 80, pp. 190–203, 2016. DOI: [10.1016/j.trac.2016.03.020](https://doi.org/10.1016/j.trac.2016.03.020).
- [50] L.-l. Feng, Y.-q. Cai, M.-c. Zhu, L.-j. Xing, and X. Wang, “The yin and yang functions of extracellular atp and adenosine in tumor immunity,” *Cancer cell international*, vol. 20, no. 1, p. 110, 2020. DOI: [10.1186/s12935-020-01195-x](https://doi.org/10.1186/s12935-020-01195-x).
- [51] B. Xiao et al., “Structure of mammalian ampk and its regulation by adp,” *Nature*, vol. 472, no. 7342, pp. 230–233, 2011. DOI: [10.1038/nature09932](https://doi.org/10.1038/nature09932).
- [52] D. Carling, C. Thornton, A. Woods, and M. J. Sanders, “Amp-activated protein kinase: New regulation, new roles?” *Biochemical Journal*, vol. 445, no. 1, pp. 11–27, 2012. DOI: [10.1042/BJ20120546](https://doi.org/10.1042/BJ20120546).
- [53] D. G. Hardie, D. Carling, and S. J. Gamblin, “Amp-activated protein kinase: Also regulated by adp?” *Trends in biochemical sciences*, vol. 36, no. 9, pp. 470–477, 2011. DOI: [10.1016/j.tibs.2011.06.004](https://doi.org/10.1016/j.tibs.2011.06.004).

- [54] A. Sharma, S. K. Anand, N. Singh, U. N. Dwivedi, and P. Kakkar, “Amp-activated protein kinase: An energy sensor and survival mechanism in the reinstatement of metabolic homeostasis,” *Experimental cell research*, vol. 428, no. 1, p. 113614, 2023. DOI: [10.1016/j.yexcr.2023.113614](https://doi.org/10.1016/j.yexcr.2023.113614).
- [55] G. R. Steinberg and D. G. Hardie, “New insights into activation and function of the ampk,” *Nature reviews Molecular cell biology*, vol. 24, no. 4, pp. 255–272, 2023. DOI: [10.1038/s41580-022-00547-x](https://doi.org/10.1038/s41580-022-00547-x).
- [56] F. Rajamohan et al., “Probing the enzyme kinetics, allosteric modulation and activation of α 1-and α 2-subunit-containing amp-activated protein kinase (ampk) heterotrimeric complexes by pharmacological and physiological activators,” *Biochemical Journal*, vol. 473, no. 5, pp. 581–592, 2016. DOI: [10.1042/BJ20151051](https://doi.org/10.1042/BJ20151051).
- [57] L. A. Booth, S. Tavallai, H. A. Hamed, N. Cruickshanks, and P. Dent, “The role of cell signalling in the crosstalk between autophagy and apoptosis,” *Cellular signalling*, vol. 26, no. 3, pp. 549–555, 2014. DOI: [10.1016/j.cellsig.2013.11.028](https://doi.org/10.1016/j.cellsig.2013.11.028).
- [58] F. Zhou, Y. Yang, and D. Xing, “Bcl-2 and bcl-xl play important roles in the crosstalk between autophagy and apoptosis,” *The FEBS journal*, vol. 278, no. 3, pp. 403–413, 2011. DOI: [10.1111/j.1742-4658.2010.07965.x](https://doi.org/10.1111/j.1742-4658.2010.07965.x).
- [59] R. Kang, H. Zeh, M. Lotze, and D. Tang, “The beclin 1 network regulates autophagy and apoptosis,” *Cell Death & Differentiation*, vol. 18, no. 4, pp. 571–580, 2011. DOI: [10.1038/cdd.2010.191](https://doi.org/10.1038/cdd.2010.191).
- [60] X. Huang et al., “Beclin 1, an autophagy-related gene, augments apoptosis in u87 glioblastoma cells,” *Oncology reports*, vol. 31, no. 4, pp. 1761–1767, 2014. DOI: [10.3892/or.2014.3015](https://doi.org/10.3892/or.2014.3015).
- [61] M. Vogler et al., “The bcl2 family: From apoptosis mechanisms to new advances in targeted therapy,” *Signal transduction and targeted therapy*, vol. 10, no. 1, p. 91, 2025. DOI: [10.1038/s41392-025-02176-0](https://doi.org/10.1038/s41392-025-02176-0).
- [62] D. L. Medina et al., “Lysosomal calcium signalling regulates autophagy through calcineurin and tfeb,” *Nature cell biology*, vol. 17, no. 3, pp. 288–299, 2015. DOI: [10.1038/ncb3114](https://doi.org/10.1038/ncb3114).
- [63] Q. Chen, J. Kang, and C. Fu, “The independence of and associations among apoptosis, autophagy, and necrosis,” *Signal transduction and targeted therapy*, vol. 3, no. 1, p. 18, 2018. DOI: [10.1038/s41392-018-0018-5](https://doi.org/10.1038/s41392-018-0018-5).

- [64] S. Liu, S. Yao, H. Yang, S. Liu, and Y. Wang, “Autophagy: Regulator of cell death,” *Cell death & disease*, vol. 14, no. 10, p. 648, 2023. DOI: [10.1038/s41419-023-06154-8](https://doi.org/10.1038/s41419-023-06154-8).
- [65] N. Mizushima, “Autophagy: Process and function,” *Genes & development*, vol. 21, no. 22, pp. 2861–2873, 2007. DOI: [10.1101/gad.1599207](https://doi.org/10.1101/gad.1599207).
- [66] L. Lei, J. Zhang, R. Wei, B. Dong, X. Wang, and Y. Zhou, “Deciphering the dual role of autophagy in gastric cancer and gastroesophageal junction cancer: From tumor suppression to cancer progression,” *Discover Oncology*, vol. 16, no. 1, p. 1013, 2025. DOI: [10.1007/s12672-025-02802-x](https://doi.org/10.1007/s12672-025-02802-x).
- [67] K. Nishida, O. Yamaguchi, and K. Otsu, “Crosstalk between autophagy and apoptosis in heart disease,” *Circulation research*, vol. 103, no. 4, pp. 343–351, 2008. DOI: [10.1161/CIRCRESAHA.108.175448](https://doi.org/10.1161/CIRCRESAHA.108.175448).
- [68] M. Li, P. Gao, and J. Zhang, “Crosstalk between autophagy and apoptosis: Potential and emerging therapeutic targets for cardiac diseases,” *International journal of molecular sciences*, vol. 17, no. 3, p. 332, 2016. DOI: [10.3390/ijms17030332](https://doi.org/10.3390/ijms17030332).
- [69] M. Su, Y. Mei, and S. Sinha, “Role of the crosstalk between autophagy and apoptosis in cancer,” *Journal of oncology*, vol. 2013, no. 1, p. 102735, 2013. DOI: [10.1155/2013/102735](https://doi.org/10.1155/2013/102735).
- [70] U. Biswas, R. Roy, S. Ghosh, and G. Chakrabarti, “The interplay between autophagy and apoptosis: Its implication in lung cancer and therapeutics,” *Cancer letters*, vol. 585, p. 216662, 2024. DOI: [10.1016/j.canlet.2024.216662](https://doi.org/10.1016/j.canlet.2024.216662).
- [71] S. Mukhopadhyay, P. K. Panda, N. Sinha, D. N. Das, and S. K. Bhutia, “Autophagy and apoptosis: Where do they meet?” *Apoptosis*, vol. 19, no. 4, pp. 555–566, 2014. DOI: [10.1007/s10495-014-0967-2](https://doi.org/10.1007/s10495-014-0967-2).
- [72] A. Thorburn, “Apoptosis and autophagy: Regulatory connections between two supposedly different processes,” *Apoptosis*, vol. 13, no. 1, pp. 1–9, 2008. DOI: [10.1007/s10495-007-0154-9](https://doi.org/10.1007/s10495-007-0154-9).
- [73] K. Moreau, S. Luo, and D. C. Rubinsztein, “Cytoprotective roles for autophagy,” *Current opinion in cell biology*, vol. 22, no. 2, pp. 206–211, 2010. DOI: [10.1016/j.ceb.2009.12.002](https://doi.org/10.1016/j.ceb.2009.12.002).
- [74] G. Marino, M. Niso-Santano, E. H. Baehrecke, and G. Kroemer, “Self-consumption: The interplay of autophagy and apoptosis,” *Nature reviews Molecular cell biology*, vol. 15, no. 2, pp. 81–94, 2014. DOI: [10.1038/nrm3735](https://doi.org/10.1038/nrm3735).

- [75] L. Zhang, Y. Zhu, J. Zhang, L. Zhang, and L. Chen, “Inhibiting cytoprotective autophagy in cancer therapy: An update on pharmacological small-molecule compounds,” *Frontiers in Pharmacology*, vol. 13, p. 966012, 2022. DOI: [10.3389/fphar.2022.966012](https://doi.org/10.3389/fphar.2022.966012).
- [76] I. Tavassoly, J. Parmar, A. Shajahan-Haq, R. Clarke, W. T. Baumann, and J. J. Tyson, “Dynamic modeling of the interaction between autophagy and apoptosis in mammalian cells,” *CPT: pharmacometrics & systems pharmacology*, vol. 4, no. 4, pp. 263–272, 2015. DOI: [10.1002/psp4.29](https://doi.org/10.1002/psp4.29).
- [77] C. Wanjek, “Systems biology as defined by nih: An intellectual resource for integrative biology,” *National Institutes of Health • Office of the Director*, vol. 19, no. 6, Nov. 2011, NIH publication. [Online]. Available: <https://doi.org/10.1128/MCB.06159-11>.
- [78] J. J. Tyson, K. C. Chen, and B. Novak, “Sniffers, buzzers, toggles and blinkers: Dynamics of regulatory and signaling pathways in the cell,” *Current opinion in cell biology*, vol. 15, no. 2, pp. 221–231, 2003. DOI: [10.1016/s0955-0674\(03\)00017-6](https://doi.org/10.1016/s0955-0674(03)00017-6).
- [79] Z. Li, S. M. Shaw, M. J. Yedwabnick, and C. Chan, “Using a state-space model with hidden variables to infer transcription factor activities,” *Bioinformatics*, vol. 22, no. 6, pp. 747–754, 2006. DOI: [10.1093/bioinformatics/btk034](https://doi.org/10.1093/bioinformatics/btk034).
- [80] P. Rangamani and R. Iyengar, “Modelling cellular signalling systems,” *Essays in Biochemistry*, vol. 45, pp. 83–94, 2008. DOI: [10.1042/BSE0450083](https://doi.org/10.1042/BSE0450083).
- [81] B. Hajdú, O. Kapuy, and T. Nagy, “Basal state calibration of a chemical reaction network model for autophagy,” *International Journal of Molecular Sciences*, vol. 25, no. 20, p. 11316, 2024. DOI: [10.3390/ijms252011316](https://doi.org/10.3390/ijms252011316).
- [82] S. Müller, C. Flamm, and P. F. Stadler, “What makes a reaction network “chemical”?” *Journal of cheminformatics*, vol. 14, no. 1, p. 63, 2022. DOI: [10.1186/s13321-022-00621-8](https://doi.org/10.1186/s13321-022-00621-8).
- [83] G. Lorenzo et al., “Patient-specific, mechanistic models of tumor growth incorporating artificial intelligence and big data,” *Annual Review of Biomedical Engineering*, vol. 26, no. 1, pp. 529–560, 2024. DOI: [10.1146/annurev-bioeng-081623-025834](https://doi.org/10.1146/annurev-bioeng-081623-025834).
- [84] L. Qiao, A. Khalilimeybodi, N. J. Linden-Santangeli, and P. Rangamani, “The evolution of systems biology and systems medicine: From mechanistic models to uncertainty quantification,” *Annual Review of Biomedical Engineering*, vol. 27, 2025. DOI: [10.1146/annurev-bioeng-102723-065309](https://doi.org/10.1146/annurev-bioeng-102723-065309).

- [85] L. Miskovic, J. Béal, M. Moret, and V. Hatzimanikatis, “Uncertainty reduction in biochemical kinetic models: Enforcing desired model properties,” *PLoS computational biology*, vol. 15, no. 8, e1007242, 2019. DOI: [10.1371/journal.pcbi.1007242](https://doi.org/10.1371/journal.pcbi.1007242).
- [86] W. W. Chen, M. Niepel, and P. K. Sorger, “Classic and contemporary approaches to modeling biochemical reactions,” *Genes & development*, vol. 24, no. 17, pp. 1861–1875, 2010. DOI: [10.1101/gad.1945410](https://doi.org/10.1101/gad.1945410).
- [87] W. Kang et al., “Time-dependent catalytic activity in aging condensates,” *Nature Communications*, vol. 16, no. 1, p. 6959, 2025. DOI: [10.1038/s41467-025-62074-5](https://doi.org/10.1038/s41467-025-62074-5).
- [88] J. L. Rendón and J. P. Pardo, “Time-dependent kinetic complexities in enzyme assays: A review,” *Biomolecules*, vol. 15, no. 5, p. 641, 2025. DOI: [10.3390/biom15050641](https://doi.org/10.3390/biom15050641).
- [89] M. Wen, E. W. C. Spotte-Smith, S. M. Blau, M. J. McDermott, A. S. Krishnapriyan, and K. A. Persson, “Chemical reaction networks and opportunities for machine learning,” *Nature Computational Science*, vol. 3, no. 1, pp. 12–24, 2023. DOI: [10.1038/s43588-022-00369-z](https://doi.org/10.1038/s43588-022-00369-z).
- [90] A. F. Villaverde, F. Fröhlich, D. Weindl, J. Hasenauer, and J. R. Banga, “Benchmarking optimization methods for parameter estimation in large kinetic models: Results supplement,” *Villaverde, AF; Fröhlich, Fabian; Weindl, Daniel; Hasenauer, Jan; Banga, Julio R.; 2018; Benchmarking optimization methods for parameter estimation in large kinetic models [Software]; Zenodo; Version 1.1*, 2018. DOI: [10.1093/bioinformatics/bty736](https://doi.org/10.1093/bioinformatics/bty736).
- [91] Y. Zhou and F. Liu, “Coordination of the ampk, akt, mtor, and p53 pathways under glucose starvation,” *International Journal of Molecular Sciences*, vol. 23, no. 23, p. 14945, 2022. DOI: [10.3390/ijms232314945](https://doi.org/10.3390/ijms232314945).
- [92] I. F. Coccimiglio and D. C. Clarke, “Adp is the dominant controller of amp-activated protein kinase activity dynamics in skeletal muscle during exercise,” *PLoS computational biology*, vol. 16, no. 7, e1008079, 2020. DOI: [10.1371/journal.pcbi.1008079](https://doi.org/10.1371/journal.pcbi.1008079).
- [93] J. R. Wiśniewski, M. Y. Hein, J. Cox, and M. Mann, “A “proteomic ruler” for protein copy number and concentration estimation without spike-in standards,” *Molecular & cellular proteomics*, vol. 13, no. 12, pp. 3497–3506, 2014. DOI: [10.1074/mcp.M113.037309](https://doi.org/10.1074/mcp.M113.037309).
- [94] T. Guo et al., “Quantitative proteome landscape of the nci-60 cancer cell lines,” *Iscience*, vol. 21, pp. 664–680, 2019. DOI: [10.1016/j.isci.2019.10.059](https://doi.org/10.1016/j.isci.2019.10.059).

- [95] D. Goodwin, R. Speth, H. Moffat, and B. Weber, *Cantera: An object-oriented software toolkit for chemical kinetics, thermodynamics, and transport processes*, <https://www.cantera.org>, Version 2.5.1, 2021.
- [96] M. Papp, T. Varga, Á. Busai, I. Zsély, T. Nagy, and T. Turányi, *Optima++ v2.5: A general c++ framework for performing combustion simulations and mechanism optimization*, <https://respecth.elte.hu/>, 2020.
- [97] S. K. Goitom et al., “Efficient numerical methods for the optimisation of large kinetic reaction mechanisms,” *Combustion Theory And Modelling*, vol. 26, no. 6, pp. 1071–1097, 2022. DOI: [10.1080/13647830.2022.2110945](https://doi.org/10.1080/13647830.2022.2110945).
- [98] O. Ledoit and M. Wolf, “A well-conditioned estimator for large-dimensional covariance matrices,” *Journal of multivariate analysis*, vol. 88, no. 2, pp. 365–411, 2004. DOI: [10.1016/S0047-259X\(03\)00096-4](https://doi.org/10.1016/S0047-259X(03)00096-4).
- [99] O. Ledoit and M. Wolf, “The power of (non-) linear shrinking: A review and guide to covariance matrix estimation,” *Journal of Financial Econometrics*, vol. 20, no. 1, pp. 187–218, 2022. DOI: [10.1093/jjfinec/nbaa007](https://doi.org/10.1093/jjfinec/nbaa007).
- [100] S. Chevallier, E. K. Kalunga, Q. Barthélémy, and E. Monacelli, “Review of riemannian distances and divergences, applied to ssvep-based bci,” *Neuroinformatics*, vol. 19, no. 1, pp. 93–106, 2021. DOI: [10.1007/s12021-020-09473-9](https://doi.org/10.1007/s12021-020-09473-9).
- [101] Y. Zhang et al., “On the properties of kullback-leibler divergence between multivariate gaussian distributions,” in *Advances in Neural Information Processing Systems*, A. Oh, T. Naumann, A. Globerson, K. Saenko, M. Hardt, and S. Levine, Eds., vol. 36, Curran Associates, Inc., 2023, pp. 58152–58165. [Online]. Available: https://proceedings.neurips.cc/paper_files/paper/2023/file/b5b4d92374323c53c24bbbc8ee0e715c-Paper-Conference.pdf.
- [102] M. Herdin, N. Czink, H. Ozcelik, and E. Bonek, “Correlation matrix distance, a meaningful measure for evaluation of non-stationary mimo channels,” in *2005 IEEE 61st vehicular technology conference*, IEEE, vol. 1, 2005, pp. 136–140. DOI: [10.1109/VETECS.2005.1543265](https://doi.org/10.1109/VETECS.2005.1543265).
- [103] J. Josse and S. Holmes, *Measures of dependence between random vectors and tests of independence. literature review*, 2014. DOI: [10.48550/arXiv.1307.7383](https://doi.org/10.48550/arXiv.1307.7383). arXiv: [1307.7383 \[stat.ME\]](https://arxiv.org/abs/1307.7383). [Online]. Available: <https://arxiv.org/abs/1307.7383>.

- [104] W. H. Koppenol and P. L. Bounds, “The warburg effect and metabolic efficiency: Recrunching the numbers,” *Science*, vol. 324, no. 5930, pp. 1029–1033, 2009. DOI: [10.1126/science.1160809](https://doi.org/10.1126/science.1160809).
- [105] A. R. Harders, P. Spellerberg, and R. Dringen, “Exogenous substrates prevent the decline in the cellular atp content of primary rat astrocytes during glucose deprivation,” *Neurochemical Research*, vol. 49, no. 5, pp. 1188–1199, 2024. DOI: [10.1007/s11064-024-04104-0](https://doi.org/10.1007/s11064-024-04104-0).
- [106] A. R. Harders, C. Arend, S. C. Denieffe, J. Berger, and R. Dringen, “Endogenous energy stores maintain a high atp concentration for hours in glucose-depleted cultured primary rat astrocytes,” *Neurochemical Research*, vol. 48, no. 7, pp. 2241–2252, 2023. DOI: [10.1007/s11064-023-03903-1](https://doi.org/10.1007/s11064-023-03903-1).
- [107] Y. Deng, D. R. Beahm, S. Ionov, and R. Sarpeshkar, “Measuring and modeling energy and power consumption in living microbial cells with a synthetic atp reporter,” *BMC biology*, vol. 19, no. 1, p. 101, 2021. DOI: [10.1186/s12915-021-01023-2](https://doi.org/10.1186/s12915-021-01023-2).
- [108] W.-H. Lin and C. Jacobs-Wagner, “Connecting single-cell atp dynamics to overflow metabolism, cell growth, and the cell cycle in escherichia coli,” *Current biology*, vol. 32, no. 18, pp. 3911–3924, 2022. DOI: [10.1016/j.cub.2022.07.035](https://doi.org/10.1016/j.cub.2022.07.035).
- [109] M. Mishra, S. Tiwari, and A. V. Gomes, “Protein purification and analysis: Next generation western blotting techniques,” *Expert review of proteomics*, vol. 14, no. 11, pp. 1037–1053, 2017. DOI: [10.1080/14789450.2017.1388167](https://doi.org/10.1080/14789450.2017.1388167).
- [110] M. I. Knight and P. J. Chambers, “Problems associated with determining protein concentration: A comparison of techniques for protein estimations,” *Molecular biotechnology*, vol. 23, no. 1, pp. 19–28, 2003. DOI: [10.1385/MB:23:1:19](https://doi.org/10.1385/MB:23:1:19).
- [111] D. Buonvicino, L. Formentini, G. Cipriani, and A. Chiarugi, “Glucose deprivation converts poly (adp-ribose) polymerase-1 hyperactivation into a transient energy-producing process,” *Journal of Biological Chemistry*, vol. 288, no. 51, pp. 36 530–36 537, 2013. DOI: [10.1074/jbc.M113.506378](https://doi.org/10.1074/jbc.M113.506378).
- [112] H. Imamura et al., “Visualization of atp levels inside single living cells with fluorescence resonance energy transfer-based genetically encoded indicators,” *Proceedings of the National Academy of Sciences*, vol. 106, no. 37, pp. 15 651–15 656, 2009. DOI: doi.org/10.1073/pnas.0904764106.

- [113] S. J. Vayttaden, S. M. Ajay, and U. S. Bhalla, “A spectrum of models of signaling pathways,” *ChemBioChem*, vol. 5, no. 10, pp. 1365–1374, 2004. DOI: [10.1002/cbic.200400127](https://doi.org/10.1002/cbic.200400127).
- [114] E. Gjerga, P. Trairatphisan, A. Gabor, and J. Saez-Rodriguez, “Literature and data-driven based inference of signalling interactions using time-course data,” *IFAC-PapersOnLine*, vol. 52, no. 26, pp. 52–57, 2019. DOI: [10.1016/j.ifacol.2019.12.235](https://doi.org/10.1016/j.ifacol.2019.12.235).
- [115] R. Eftimie, J. J. Gillard, and D. A. Cantrell, “Mathematical models for immunology: Current state of the art and future research directions,” *Bulletin of mathematical biology*, vol. 78, no. 10, pp. 2091–2134, 2016. DOI: [10.1007/s11538-016-0214-9](https://doi.org/10.1007/s11538-016-0214-9).
- [116] C. Ludwig, M. Claassen, A. Schmidt, and R. Aebersold, “Estimation of absolute protein quantities of unlabeled samples by selected reaction monitoring mass spectrometry,” *Molecular & Cellular Proteomics*, vol. 11, no. 3, pp. M111-013987, 2012. DOI: [10.1074/mcp.M111.013987](https://doi.org/10.1074/mcp.M111.013987).
- [117] T. A. Butler, J. W. Paul, E.-C. Chan, R. Smith, and J. M. Tolosa, “Misleading westerns: Common quantification mistakes in western blot densitometry and proposed corrective measures,” *BioMed research international*, vol. 2019, no. 1, p. 5214821, 2019. DOI: [10.1155/2019/5214821](https://doi.org/10.1155/2019/5214821).
- [118] A. Maestri et al., “Titration-wb: A methodology for accurate quantitative protein determination overcoming reproducibility errors,” *PLoS One*, vol. 20, no. 6, e0325052, 2025. DOI: [10.1371/journal.pone.0325052](https://doi.org/10.1371/journal.pone.0325052).
- [119] P. Loskot, K. Atitey, and L. Mihaylova, “Comprehensive review of models and methods for inferences in bio-chemical reaction networks,” *Frontiers in genetics*, vol. 10, p. 549, 2019. DOI: [10.3389/fgene.2019.00549](https://doi.org/10.3389/fgene.2019.00549).
- [120] E. D. Mitra, R. Dias, R. G. Posner, and W. S. Hlavacek, “Using both qualitative and quantitative data in parameter identification for systems biology models,” *Nature communications*, vol. 9, no. 1, p. 3901, 2018. DOI: [10.1038/s41467-018-06439-z](https://doi.org/10.1038/s41467-018-06439-z).
- [121] P. Marambio et al., “Glucose deprivation causes oxidative stress and stimulates aggresome formation and autophagy in cultured cardiac myocytes,” *Biochimica et Biophysica Acta (BBA)-Molecular Basis of Disease*, vol. 1802, no. 6, pp. 509–518, 2010. DOI: [10.1016/j.bbadi.2010.02.002](https://doi.org/10.1016/j.bbadi.2010.02.002).
- [122] J. F. Moruno-Manchón, E. Perez-Jimenez, and E. Knecht, “Glucose induces autophagy under starvation conditions by a p38 mapk-dependent pathway,” *Biochemical Journal*, vol. 449, no. 2, pp. 497–506, 2013. DOI: [10.1042/BJ20121122](https://doi.org/10.1042/BJ20121122).

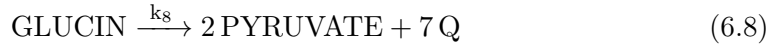
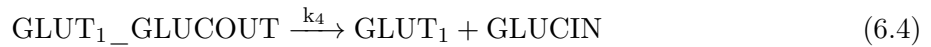
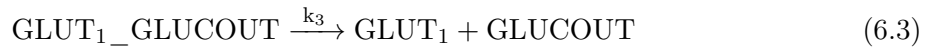
- [123] C. López-Otín, M. A. Blasco, L. Partridge, M. Serrano, and G. Kroemer, “Hallmarks of aging: An expanding universe,” *Cell*, vol. 186, no. 2, pp. 243–278, 2023. DOI: [10.1016/j.cell.2022.11.001](https://doi.org/10.1016/j.cell.2022.11.001).
- [124] A. Salminen and K. Kaarniranta, “Amp-activated protein kinase (ampk) controls the aging process via an integrated signaling network,” *Ageing research reviews*, vol. 11, no. 2, pp. 230–241, 2012. DOI: [10.1016/j.arr.2011.12.005](https://doi.org/10.1016/j.arr.2011.12.005).
- [125] J. B. Mannick and D. W. Lamming, “Targeting the biology of aging with mtor inhibitors,” *Nature aging*, vol. 3, no. 6, pp. 642–660, 2023. DOI: [10.1038/s43587-023-00416-y](https://doi.org/10.1038/s43587-023-00416-y).
- [126] R. Khandia et al., “A comprehensive review of autophagy and its various roles in infectious, non-infectious, and lifestyle diseases: Current knowledge and prospects for disease prevention, novel drug design, and therapy,” *Cells*, vol. 8, no. 7, p. 674, 2019. DOI: [10.3390/cells8070674](https://doi.org/10.3390/cells8070674).
- [127] M. S. Uddin et al., “Autophagy and alzheimer’s disease: From molecular mechanisms to therapeutic implications,” *Frontiers in aging neuroscience*, vol. 10, p. 04, 2018. DOI: [10.3389/fnagi.2018.00004](https://doi.org/10.3389/fnagi.2018.00004).
- [128] J.-L. Chen et al., “Autophagy inhibitors for cancer therapy: Small molecules and nanomedicines,” *Pharmacology & therapeutics*, vol. 249, p. 108485, 2023. DOI: [10.1016/j.pharmthera.2023.108485](https://doi.org/10.1016/j.pharmthera.2023.108485).
- [129] M. Su, Z. Zhang, L. Zhou, C. Han, C. Huang, and E. C. Nice, “Proteomics, personalized medicine and cancer,” *Cancers*, vol. 13, no. 11, p. 2512, 2021. DOI: [10.3390/cancers13112512](https://doi.org/10.3390/cancers13112512).
- [130] T. Saleh, L. Cuttino, and D. A. Gewirtz, “Autophagy is not uniformly cytoprotective: A personalized medicine approach for autophagy inhibition as a therapeutic strategy in non-small cell lung cancer,” *Biochimica et Biophysica Acta (BBA)-General Subjects*, vol. 1860, no. 10, pp. 2130–2136, 2016. DOI: [10.1016/j.bbagen.2016.06.012](https://doi.org/10.1016/j.bbagen.2016.06.012).
- [131] I. Grosjean et al., “Autophagopathies: From autophagy gene polymorphisms to precision medicine for human diseases,” *Autophagy*, vol. 18, no. 11, pp. 2519–2536, 2022. DOI: [10.1080/15548627.2022.2039994](https://doi.org/10.1080/15548627.2022.2039994).
- [132] M.-S. Kim et al., “A draft map of the human proteome,” *Nature*, vol. 509, no. 7502, pp. 575–581, 2014. DOI: [10.1038/nature13302](https://doi.org/10.1038/nature13302).

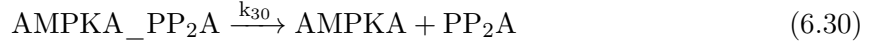
- [133] S. A. John, M. Ottolia, J. N. Weiss, and B. Ribalet, “Dynamic modulation of intracellular glucose imaged in single cells using a fret-based glucose nanosensor,” *Pflügers Archiv-European Journal of Physiology*, vol. 456, no. 2, pp. 307–322, 2008. DOI: [10.1007/s00424-007-0395-z](https://doi.org/10.1007/s00424-007-0395-z).
- [134] R. Arce-Molina et al., “A highly responsive pyruvate sensor reveals pathway-regulatory role of the mitochondrial pyruvate carrier mpc,” *eLife*, vol. 9, e53917, 2020. DOI: [10.7554/eLife.53917](https://doi.org/10.7554/eLife.53917).

Supplementary Material

6.1. Defined Reactions and Corresponding Rate Constants

The reactions defined in our model are listed below from eq. (6.1) to eq. (6.77). The corresponding k_i rate constants are provided in Table 6.1. The sources for the reactions are the same as they are for the corresponding rate constants. The right side of the first equation (eq. 6.1) corresponds to cells of the well that are not modeled but in an experiment would still be consuming glucose and thus influence the concentrations of GLUCOUT, which corresponds to glucose in the whole cell culture.





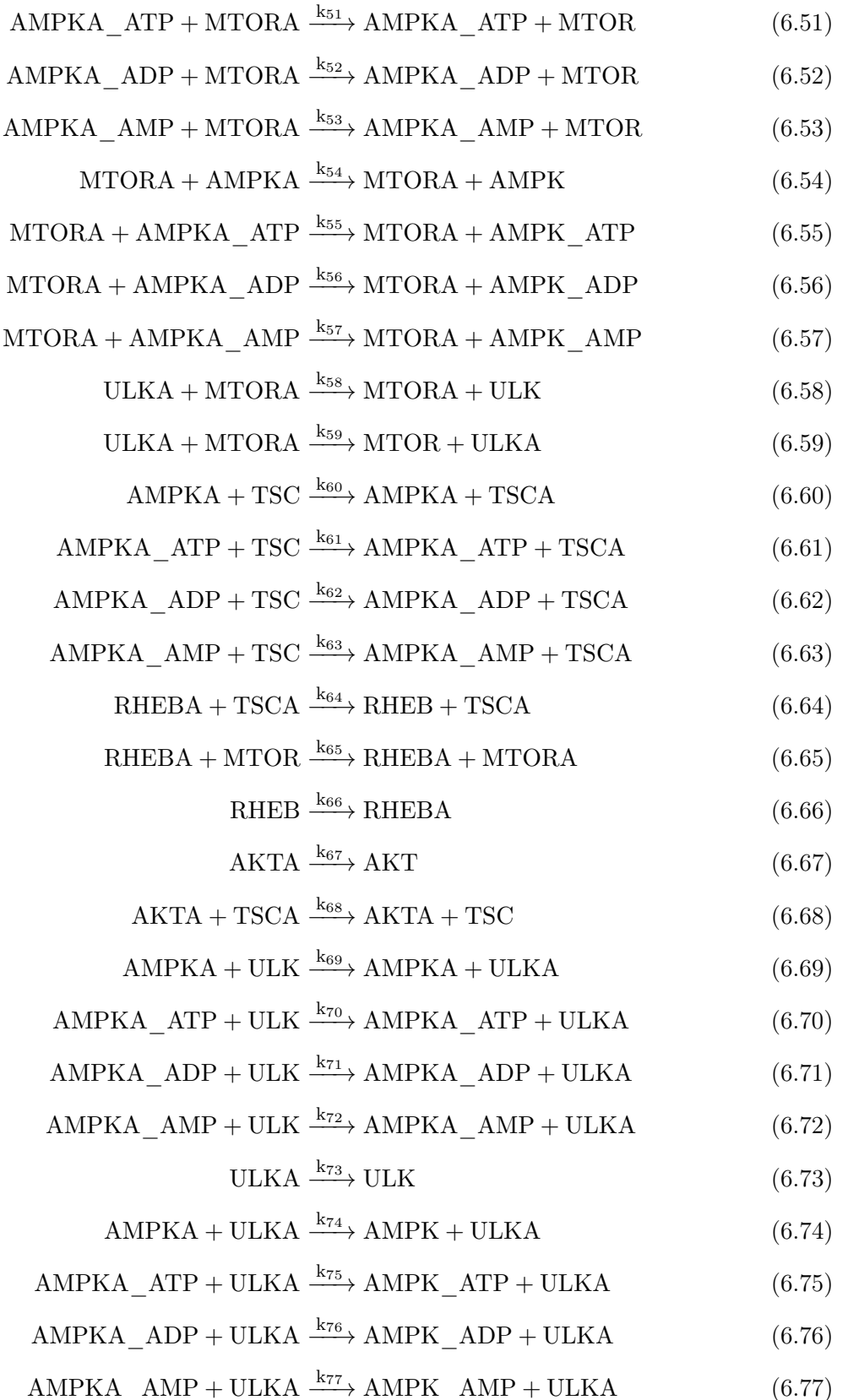


Table 6.1: The original and calibrated rate constants used in the model are provided in this table. The values are given using scientific notation (i.e., E-08 represents 10^{-8}) in units of $\frac{1}{s}$ for first order rate constants and in units of $\frac{cm^3}{mol \cdot s}$ for rates of second order reactions. The original value corresponds to the one derived from the literature, while the calibrated value represents the revised constants that we used in our simulations. Revision of rate constants was guided by ensuring the stability of the basal state statistical calculations (refer to Section 3.2.3.2) as well as by trial and error to represent biologically realistic qualitative dynamics.

Rate constant	Original value	Calibrated value	Source
k_1	2.5E-08	2.5E-08	calibrated
k_2	1.28E+06	1.28E+06	Zhou et al. [91]
k_3	1.553	0.555	Zhou et al. [91]
k_4	0.111	0.111	Zhou et al. [91]
k_5	1.28E+06	1.28E+06	Zhou et al. [91]
k_6	1.553	0.555	Zhou et al. [91]
k_7	0.111	0.111	Zhou et al. [91]
k_8	4E-05	4E-05	calibrated
k_9	4E-05	4E-05	calibrated
k_{10}	1.0E+06	1.0E+06	calibrated
k_{11}	1.3E-04	6.15E-05	Zhou et al. [91]
k_{12}	1.67E+07	1.67E+05	Zhou et al. [91]
k_{13}	1.67E+07	1.67E+04	Zhou et al. [91]
k_{14}	1E+06	1E+06	Coccimiglio et al. [92]
k_{15}	2.2E-01	2.2E-01	Coccimiglio et al. [92]
k_{16}	1.5E+06	1.5E+06	Coccimiglio et al. [92]
k_{17}	2.25E-03	2.25E-03	Coccimiglio et al. [92]
k_{18}	1.5E+06	1.5E+06	Coccimiglio et al. [92]
k_{19}	3.75E-03	3.75E-03	Coccimiglio et al. [92]
k_{20}	1E+06	1E+06	Coccimiglio et al. [92]
k_{21}	4E-01	4E-01	Coccimiglio et al. [92]
k_{22}	1.5E+06	1.5E+06	Coccimiglio et al. [92]
k_{23}	2.25E-03	2.25E-03	Coccimiglio et al. [92]
k_{24}	1E+06	1E+06	Coccimiglio et al. [92]
k_{25}	3.75E-03	3.75E-03	Coccimiglio et al. [92]
k_{26}	3.61E+06	3.61E+06	Coccimiglio et al. [92]
k_{27}	5E+03	5E+03	Coccimiglio et al. [92]
k_{28}	5E+01	5E+01	Coccimiglio et al. [92]
k_{29}	8.21E+06	8.21E+06	Coccimiglio et al. [92]
k_{30}	5E+02	5E+02	Coccimiglio et al. [92]
k_{31}	5E+01	5E+01	Coccimiglio et al. [92]
k_{32}	3.61E+06	3.61E+06	Coccimiglio et al. [92]
k_{33}	5E+03	5E+03	Coccimiglio et al. [92]
k_{34}	5E+01	5E+00	Coccimiglio et al. [92]
k_{35}	8.21E+06	8.21E+06	Coccimiglio et al. [92]
k_{36}	5E+02	5E+02	Coccimiglio et al. [92]
k_{37}	5E+01	5E+02	Coccimiglio et al. [92]
k_{38}	5.41E+06	5.41E+06	Coccimiglio et al. [92]
k_{39}	7.5E+03	7.5E+01	Coccimiglio et al. [92]

Table 1 Continued: The original and calibrated rate constants used in the model are provided in this table. The values are given using scientific notation (i.e., E-08 represents 10^{-8}) in units of $\frac{1}{s}$ for first order rate constants and in units of $\frac{cm^3}{mol \cdot s}$ for rates of second order reactions. The original value corresponds to the one derived from the literature, while the calibrated value represents the revised constants that we used in our simulations. Revision of rate constants was guided by ensuring the stability of the basal state statistical calculations (refer to Section 3.2.3.2) as well as by trial and error to represent biologically realistic qualitative dynamics.

Rate constant	Original value	Calibrated value	Source
k_{40}	7.5E+01	1.5E+02	Coccimiglio et al. [92]
k_{41}	8.21E+04	8.21E+04	Coccimiglio et al. [92]
k_{42}	5E+00	5E+00	Coccimiglio et al. [92]
k_{43}	1E+00	1E+00	Coccimiglio et al. [92]
k_{44}	1.44E+07	1.44E+07	Coccimiglio et al. [92]
k_{45}	2E+04	2E+01	Coccimiglio et al. [92]
k_{46}	2E+02	3E+02	Coccimiglio et al. [92]
k_{47}	8.21E+04	8.21E+04	Coccimiglio et al. [92]
k_{48}	5E+00	5E+00	Coccimiglio et al. [92]
k_{49}	1E+00	1E+00	Coccimiglio et al. [92]
k_{50}	8.01423E+07	8.01423E+07	Coccimiglio et al. [81]
k_{51}	8.01423E+07	8.01423E+07	Coccimiglio et al. [81]
k_{52}	8.01423E+07	8.01423E+07	Coccimiglio et al. [81]
k_{53}	4.54269E+08	4.54269E+08	Coccimiglio et al. [81]
k_{54}	9.6385E+03	9.6385E+03	Coccimiglio et al. [81]
k_{55}	9.6385E+03	9.6385E+03	Coccimiglio et al. [81]
k_{56}	9.6385E+03	9.6385E+03	Coccimiglio et al. [81]
k_{57}	9.6385E+03	9.6385E+03	Coccimiglio et al. [81]
k_{58}	1.6122E+04	1.6122E+04	Coccimiglio et al. [81]
k_{59}	1.9507E+05	1.9507E+05	Coccimiglio et al. [81]
k_{60}	1.489E+03	1.489E+03	Coccimiglio et al. [81]
k_{61}	1.489E+03	1.489E+03	Coccimiglio et al. [81]
k_{62}	1.5342E+03	1.5342E+03	Coccimiglio et al. [81]
k_{63}	1.3537E+04	1.3537E+04	Coccimiglio et al. [81]
k_{64}	5.2292E+03	5.2292E+03	Coccimiglio et al. [81]
k_{65}	1.4312E+08	1.4312E+08	Coccimiglio et al. [81]
k_{66}	9.2104E-08	9.2104E-08	Coccimiglio et al. [81]
k_{67}	5.0667E-07	5.0667E-07	Coccimiglio et al. [81]
k_{68}	6.4680E+09	6.4680E+09	Coccimiglio et al. [81]
k_{69}	4.0270E+03	3.3223E+05	Coccimiglio et al. [81]
k_{70}	4.0270E+03	3.3223E+05	Coccimiglio et al. [81]
k_{71}	4.0270E+03	3.423E+05	Coccimiglio et al. [81]
k_{72}	4.0270E+03	1.2203E+06	Coccimiglio et al. [81]
k_{73}	2.8119E-05	2.8119E-05	Coccimiglio et al. [81]
k_{74}	2.5661E+04	4.1653E+01	Coccimiglio et al. [81]
k_{75}	2.6661E+04	4.1653E+01	Coccimiglio et al. [81]
k_{76}	2.6661E+04	4.1653E+01	Coccimiglio et al. [81]
k_{77}	2.6661E+04	4.1653E+01	Coccimiglio et al. [81]

6.2. Initial Conditions

Table 6.2: The table presents the basal state initial condition ranges for our simulations. . The IC of each species for any given simulation is randomly generated around the species mean (3. column) for both basal and starvation conditions. The random sampling range for a species s is defined as follows: $[0.5 \cdot \bar{x}_s, 1.5 \cdot \bar{x}_s]$, where \bar{x}_s denotes the species' mean concentration. In columns min and max, the lower and upper bounds of the literature-derived concentration ranges are provided. The units for each concentration value are $\frac{mol}{cm^3}$. An IC of 0 $\frac{mol}{cm^3}$ is assumed for all enzyme-substrate Michaelis-Menten complexes (bottom 10 rows). Initial Conditions for GLUCOUT depend on the experimental conditions and is an input of the system: for starvation the concentration is set at $1E - 6 \frac{mol}{cm^3}$, while for basal-state simulations, the input is $6E - 6 \frac{mol}{cm^3}$. Similarly for Q (the proton motive force), in starvation the IC $1E - 9 \frac{mol}{cm^3}$, whereas in homeostatic simulations it is $3E - 6 \frac{mol}{cm^3}$. Sources for each IC are also provided. The descriptor column specifies if the species was used for basal state statistics (please refer to section 3.2.3.2)

species	min $\frac{mol}{cm^3}$	mean $\frac{mol}{cm^3}$	max $\frac{mol}{cm^3}$	source	descriptor
GLUT1	1.47E-10	1.99E-10	2.57E-10	[132]	yes
GLUCIN	8.50E-08	4.00E-07	5.50E-07	[133]	yes
ATP	3.00E-06	5.00E-06	7.00E-06	[48], [49], [50]	yes
ADP	5.00E-08	1.25E-07	2.00E-07	[92]	yes
AMP	5.00E-10	2.50E-09	5.00E-09	[92]	yes
AMPK	1.00E-10	1.00E-10	1.00E-10	[81]	yes
AMPKA	0	0	0	[81]	yes
AMPK_ATP	1.00E-10	1.00E-10	1.00E-10	[81]	yes
AMPK_ADP	1.00E-10	1.00E-10	1.00E-10	[81]	yes
AMPK_AMP	1.00E-10	1.00E-10	1.00E-10	[81]	yes
AMPKA_ATP	0.00E+00	0.00E+00	0.00E+00	[92]	yes
AMPKA_ADP	0.00E+00	0.00E+00	0.00E+00	[92]	yes
AMPKA_AMP	0.00E+00	0.00E+00	0.00E+00	[92]	yes
LKB1	2.13E-11	2.88E-11	3.72E-11	[132]	yes
PP2A	2.86E-10	3.86E-10	4.98E-10	[132]	yes
PYRUVATE	2.00E-08	3.30E-08	4.00E-08	[134]	no
AKT	0.00E+00	0.00E+00	0.00E+00	[81]	yes
AKTA	5.00E-11	1.00E-10	2.00E-10	[81]	yes
MTOR	0.00E+00	0.00E+00	0.00E+00	[81]	yes
MTORA	1.88E-10	3.75E-10	7.50E-10	[81]	yes
RHEB	0.00E+00	0.00E+00	0.00E+00	[81]	yes
RHEBA	1.50E-10	3.00E-10	6.00E-10	[81]	yes
TSC	1.13E-10	2.25E-10	4.50E-10	[81]	yes
TSCA	0.00E+00	0.00E+00	0.00E+00	[81]	yes

species	min [$\frac{mol}{cm^3}$]	mean [$\frac{mol}{cm^3}$]	max [$\frac{mol}{cm^3}$]	source	descriptor
ULK	3.50E-11	7.00E-11	1.40E-10	[81]	yes
ULKA	0	0	0	[81]	yes
AMPK_LKB1	0	0	0	assumed	no
AMPK_ATP_LKB1	0	0	0	assumed	no
AMPK_ADP_LKB1	0	0	0	assumed	no
AMPK_AMP_LKB1	0	0	0	assumed	no
AMPKA_PP2A	0	0	0	assumed	no
AMPKA_ATP_PP2A	0	0	0	assumed	no
AMPKA_ADP_PP2A	0	0	0	assumed	no
AMPKA_AMP_PP2A	0	0	0	assumed	no
GLUT1_GLUCOUT	0	0	0	assumed	no
GLUT1_GLUCIN	0	0	0	assumed	no
input	basal	starvation		source	no
GLUCOUT	6E-6	1E-6		[45]	yes
Q	3E-6	1E-9		[45]	no